

2009

Thermal and mechanical phenomena in nanoscale constrained domains

Liyang Guo
Iowa State University

Follow this and additional works at: <https://lib.dr.iastate.edu/etd>

 Part of the [Mechanical Engineering Commons](#)

Recommended Citation

Guo, Liyang, "Thermal and mechanical phenomena in nanoscale constrained domains" (2009). *Graduate Theses and Dissertations*. 10702.

<https://lib.dr.iastate.edu/etd/10702>

This Thesis is brought to you for free and open access by the Iowa State University Capstones, Theses and Dissertations at Iowa State University Digital Repository. It has been accepted for inclusion in Graduate Theses and Dissertations by an authorized administrator of Iowa State University Digital Repository. For more information, please contact digirep@iastate.edu.

Thermal and mechanical phenomena in nanoscale constrained domains

by

LiYing Guo

A thesis submitted to the graduate faculty
in partial fulfillment of the requirements for the degree of
MASTER OF SCIENCE

Major: Mechanical Engineering

Program of Study Committee:
Xinwei Wang, Major Professor
Palaniappa A. Molian
Zhijian Wang

Iowa State University

Ames, Iowa

2009

Table of Contents

LIST OF FIGURES	iii
LIST OF TABLES	v
ACKNOWLEDGEMENT	vi
ABSTRACT	viii
CHAPTER 1: INTRODUCTION	1
1.1 Introduction to thermal and mechanical phenomena in nanoscale laser-material interaction	1
1.2 Thermal Transport in TiO ₂ nanotube arrays	3
CHAPTER 2: BASICS OF MD SIMULATION	6
2.1 Theoretical introduction to MD simulation	6
2.2 Parallel computation	11
2.3 Laser material interaction	12
CHAPTER 3: SHOCK WAVE IN LASER-INDUCED NANOMANUFACTURING	16
3.1. Evolution of shockwave front	19
3.2. Evolution of the interaction zone	25
3.3. Energy exchange between plume and ambient gas in the shockwave	30
3.4. Conclusion	34
CHAPTER 4: EXPERIMENTAL DETAIL FOR STUDYING NANOSCALE THERMAL TRANSPORT	35
4.1 Sample preparation	35
4.2 Experiment principles	36
CHAPTER 5: NANOSCALE THERMAL TRANSPORT IN TiO₂ NANOTUBE ARRAYS	41
CHAPTER 6: FUTURE WORK	48
REFERENCES	50
RELATED PUBLICATIONS	54

LIST OF FIGURES

Figure2. 1	Cell structure and linked list in 2-D plate	9
Figure2. 2	Schematic of the MD configuration for shock wave study and parallel computation (Domain sizes under different conditions are listed in Table 3).	12
Figure2. 3	Schematic of the laser beam absorption in the material.	15
Figure 3. 1	Evolution of atomic positions during shock wave formation and propagation (different cases at different time instants are listed in the column). Each dot in the figure represents an atom. Red dots: target atoms; blue dots: ambient gas atoms. Horizontal coordinate: y coordinate in the simulation (0-900 nm). Vertical coordinate: z coordinate in the simulation (50-595 nm)	17
Figure 3. 2	Movements of target atoms and ambient gas atoms (black dots and blue lines represent target atoms and their speed; red dots and pink lines represent ambient gas atoms and their speed).	21
Figure 3. 3	Shock wave front positions (a) and velocities (b) in different ambient gases. In figure (a), the solid lines are the fitting curve of the MD data.	28
Figure 3. 4	Decay of the Mach number of the shock wave front propagation in different ambient gases.	29
Figure 3. 5	Evolution of the interaction zone area under the influence of different β and $\tilde{\gamma}$	29
Figure 3. 6	Kinetic energy of ejected atoms and kinetic energy change of ambient gas atoms: (a) under different molecular mass ratios ($\gamma \neq 1$); (b) under different gas pressures ($\beta = 1$).	31
Figure 3. 7	Material ablated under the influence of different β and $\tilde{\gamma}$	32
Figure 4. 1	Schematic structure of the TiO ₂ nanotube arrays. (a) General structure for TiO ₂ nanotubes fabricated on Ti substrate. From top to bottom, the layers are gold coating, TiO ₂ nanowires, TiO ₂ nanotubes, and Ti substrate; (b) Sample 1 for the PT experiment; (c) Freestanding TiO ₂ nanotube arrays sample for TET experiment. The figures are not	

- to scale. 38
- Figure 4. 2 The measured phase shift of surface temperature variation in the PT experiment versus the fitting results for the TiO₂ nanotube arrays (Sample 1: 29.2 μm thick). 39
- Figure 4. 3 Schematic of the heat flow direction along the cross-tube direction. The inset is the SEM image of the top view of TiO₂ nanotube arrays from work done by Jun's *et.al.*¹ L_α and L_β are the calculation units in α and β paths. W_\square and W_\square are the width of the two paths. 40
- Figure 5. 1 Normalized temperature increase versus the fitting results for the TiO₂ nanotube arrays in the cross-tube direction, measured by TET experiments. The solid lines are the theoretical values for each sample. The circles are the experimental data measured for sample 2-a and the triangles are the experimental data for sample 2-b. The insets are the sample pictures under microscope. 44

LIST OF TABLES

Table 2. 1	Non-dimensionalized parameters	10
Table 2. 2	Values of the parameters used in the simulation	13
Table 2. 3	Sound speed and pressure under ideal gas assumption	14
Table 3. 1	Conditions, domain sizes and total number of atoms for different groups	18

ACKNOWLEDGEMENT

There are many people I would like to thank for making my years at Iowa State University fulfilling. First and foremost, I would like to thank Dr. Xinwei Wang for the opportunity to work in his laboratory, for his guidance, encouragement, patience, support and for being a role model more than just academics.

I also would like to thank my program of study committee members, Dr. Palaniappa A. Molian and Dr. Zhijian Wang for their advice, feedback and help. I am grateful to Jun Wang, Dr. Zhiqun Lin and his laboratory staff for providing various testing samples in my project.

My special thanks to all my lab-mates and office-mates, especially Jiaqi Guo, Lijun Zhang and Longzhang Tian for their advice and valuable assistance in trouble shooting, Xuhui Feng, Tao Wang and Sobieslaw Gacek for their support in research, Xiangwen Chen, Xiaopeng Huang, Yanan Yue, Ruben Flesner, Lin Liu, and Yufeng Wu for their support and friendship. I would like also thank Dr. Matthew Hagge for his advices during my teaching assistant duty. I give my heartfelt thanks to the Mechanical Engineering Department for providing such a great academic environment here and for the efforts to encourage female students.

Most importantly I thank my parents, my brother and his family for believing in me and never expecting anything less of me and for being my support all the time.

ABSTRACT

In the manufacturing area, the laser has attracted increasing attention in recent year as an important tool in the practice of micro/nano scale manufacturing, such as surface microfabrication and processing, pulsed laser deposition of films and coatings, laser machining of metals and non-metallic materials, and laser surface cleaning. During the laser assisted nanostructuring process, intensive heating will cause the material to experience fast phase change that the non-equilibrium state will lead to shock wave near the heating spot. In nanostructures, thermal movements of molecules/atoms show strong statistical variations in space since the equilibrium state cannot be established. Molecular dynamics (MD) simulation, which directly tracks the movements of molecules/atoms, is capable of exploring physical phenomena down to molecular/atomic levels and predicting processes under different conditions. The previous work done in our group have investigated the evolution of density, temperature, pressure, and shock wave front Mach number. Chapter 2 is an introduction to the basics of MD simulation. In chapter 3, the evolution of the interaction zone and energy exchange between the plume and the ambient gas are studied with respect to different gas/solid molecular mass ratios and different ambient gas densities. The evolutions of shock wave front position as well as velocity and Mach number in different ambient gases are also studied.

Lasers also have wide spread popularity in characterization physical properties of materials. When illuminating the surface of materials, the laser light can be absorbed by the material and cause the temperature and thermal radiation variation at the surface. These phenomena have been intensively studied in the past. A photothermal (PT) technique has been developed in our group for characterizing thermal physical properties of different materials. For the thermal properties characterization of amorphous titanium dioxide (TiO₂) nanotube arrays, this technique provides the experimental data of the as-prepared sample density and the thermal conductivity along the tube length direction. The thermal conductivity in the cross-tube direction is measured by the transient electrothermal (TET) technique. Combining the two techniques, the contact resistance between the TiO₂ nanotubes is also investigated. Chapter 4 is for the experimental setup for the studying of nanoscale thermal transport. Chapter 5 analyzes the experimental data in detail and compares with work done by other researchers.

The emphasis of future work is outlined and described in Chapter 6.

CHAPTER 1: INTRODUCTION

1.1 Introduction to thermal and mechanical phenomena in nanoscale laser-material interaction

Since the first laser was demonstrated in 1960, lasers have found applications in many areas, among which laser assisted manufacturing has attracted considerable attention in recent years. A number of laser-assisted manufacturing techniques have been developed to handle the dimension decreasing materials and surfaces. Conventional optical maskless manufacturing techniques use focused narrow beam to directly write into materials, which are convenient yet restricted by the diffraction limit. Using apertures or masks can help to further reduce the limit, but the cost for updating with new generation of technology will continue to escalate and even become prohibitive for low volume products. As an alternative, one has to use extreme UV radiation (10-100 nm) or soft x-rays to manufacture structures in the nanometer range [1]. A large amount of work has been done to extend the resolution limit and provide tools and ultrasmall optoelectronic devices for nanomanufacturing such as nanofabricating, nanolithography and nanomodification [2-10]. Near-field scanning optical microscope (NSOM) works with resolutions from 10 to 100 nm with apertures and 1 to 20 nm without apertures [11-13]. The superlens is capable of imaging features with 60 nm or 1/6

of the illumination wavelength [14]. As one approach that attracted enormous interests in the past decade, the laser-assisted scanning probe microscope (SPM) has been shown to be effective for processing materials and surface at nanoscales. When irradiated by a pulsed laser, the SPM tip could create a significantly enhanced optical field with two orders of magnitude [15] enhancement. With a femtosecond laser, a resolution down to 10 nm could be achieved [16]. Using an atomic force microscope (AFM) combined with a 532 nm pulsed laser, surface structure with a lateral resolution of 1.5-7 nm has been created [17].

During the process of laser-assisted SPM nanostructuring, intensive laser heating will make the solid-state material directly transfer into gas phase to result in phase explosion as a consequence of insufficient time for normal boiling to take place [18]. This often leads to a shock wave when an ambient gas is present during the process. Owing to the increasing interests in nanomanufacturing, there have been studies on properties of the expansion plume and its strong interactions with the ambient gas, analytically, experimentally and numerically. In Zhang's work, a one dimensional model was established to describe the shock wave front [19]. Jeong *et al.* [20] investigated the correlation between the transit time and location of the laser-induced shock wave and compared the conversion efficiency with the conventional blast wave. Kohen and Martens [21] simulated the process of a pump laser exciting an impurity molecule embedded in a solid host to a repulsive electronic state. Their work provided a direct view of the generation and propagation of nanoscale shock waves.

In nanostructures, thermal movements of molecules/atoms show strong statistical variations in space since the equilibrium state cannot be established. Molecular dynamics (MD) simulation, which directly tracks the movements of molecules/atoms, is capable of exploring physical phenomena down to molecular/atomic levels. Wang's previous work explored the thermal and mechanical phenomena beneath the sample surface by tracking over 200 million atoms [22] and studied the solidification and epitaxial regrowth in surface nanostructuring [23]. Feng's work on nanodomain shock wave was focused on the interface properties of the shock wave front during its propagation [24]. However, none of the previous studies gives consideration of the effects of the molecular weight and density of ambient gas on shock wave in laser-induced nanostructuring.

In chapter 2 and chapter 3, MD simulations are conducted to track the trajectory of over 2 million atoms. The evolution of the interaction zone and energy exchange between the plume and the ambient gas are studied with respect to different gas/solid molecular mass ratios and different ambient gas densities. The evolution of shock wave front position as well as velocity and Mach number in different ambient gases are also studied.

1.2 Thermal Transport in TiO₂ nanotube arrays

In recent years, TiO₂ has attracted increasing interest as an environmental cleaning

ceramic material, and has been fabricated into nanostructures such as nanoparticles, thin films, and nanofibers. Highly ordered, vertically oriented, free standing TiO_2 nanotube arrays fabricated by anodization have received considerable attention due to its unique structure of high surface-to-volume and length-to-diameter ratios. Three generations of techniques have been developed in the past to produce TiO_2 nanotube arrays [25]. Studies were also carried out on the fabrication of TiO_2 nanotube arrays on different substrates to suite varied applications[25-27]. These techniques have enabled the production of TiO_2 nanotube arrays with various pore to pore distance, diameter and wall thickness through controlling the water content, pH value, voltage, and temperature [25, 27-28]. TiO_2 nanotube arrays with length from several hundred nanometers to one millimeter have been fabricated successfully [29]. Owing to their narrower band gap and remarkable architecture, TiO_2 nanotubes have the great potential to control the lateral spacing geometry and regulate cell fate [27], to utilize visible light energy, to enhance electron transport and suppress recombination, and to provide large sensing and reacting areas [30-32]. To date, TiO_2 nanotubes have been applied to various areas including biomedical implant devices [27], biomedical diagnostic applications, gas sensors, solar cells, fuel cells, lean-burn gasoline engines, and photocatalyst [33-38].

Concerns have arisen about severe thermal issues in fabricating and functioning of TiO_2 nanotube arrays due to extremely localized electrical, optical, and mechanical heating.

Different thermal response of the base material and TiO_2 nanotube arrays could lead to

material interface sliding, structure degrading, efficiency downgrading, and mechanical failure. To predict, evaluate, and improve the thermal performance of TiO₂ nanotube arrays during their fabrication and engineering applications, solid experimental data about the thermophysical properties of such nanostructures becomes extremely important. Thermal properties of a material down to micro/nanoscale can be dramatically different from those of the bulk counterpart [39]. In the past, little work has been done with respect to the thermal management in the applications of TiO₂ nanotube arrays. In this work, we report the experimental characterization of anisotropic thermophysical properties of highly-ordered TiO₂ nanotube arrays and pioneer the evaluation of thermal contact resistance between TiO₂ nanotubes by using our recently developed transient-electro-thermal (TET) technique [40] and photo-thermal (PT) method [41]. Two samples of highly-ordered TiO₂ nanotube arrays are characterized. The TiO₂ tubes in them have an average inner diameter, center-to-center distance, and wall thickness of 90 nm, 120 nm, and 15 nm, respectively. Sample 1 is about 29.2 μm and sample 2 is about 140 μm in tube length.

CHAPTER 2: BASICS OF MD SIMULATION

2.1 Theoretical introduction to MD simulation

The modeled system is an argon thin film positioned in a gas environment. Initially, the system is equilibrated at the designated temperature 50 K for 200 ps. A pulsed laser is then focused on the center of the film for 30 ps. The process is recorded from the beginning until 1 ns. The objective is to investigate the effect of the molecular weight and density of ambient gas on the laser induced shock wave. Eight cases are studied in two groups. Group one has the same ambient gas pressure but different molecular mass ratios of gas to solid. This is designed to reflect the effect of environment molecular mass on the shock wave rather than to recover a practical experimental condition. Group two uses the same ambient gas molecular weight but different ambient gas pressures. For ease of discussion, β is used to represent the molecular mass ratio of gas to solid, which has the form of $\beta = M_{\text{gas}} / M_{\text{solid}}$, where M_{gas} and M_{solid} are the molecular mass of the ambient gas and the target solid. γ represents the ratio of the ambient gas pressure to a reference pressure (0.217 MPa), which is expressed as $\gamma = p_{\text{ambient}} / p_{\text{ref}}$.

A modified quasi three dimensional domain from our previous work is established in this study. The construction of solid target in each case is basically 5 face-centered-cubes

(FCCs) in the x direction, 1700 or 1664 FCCs in the y direction and 60 FCCs in the z direction for group 1, and 1664 FCCs in the y direction and 64 FCCs in the z direction for group 2. The lattice constant for each FCC cell is 5.414 Å.

In MD simulation, the dynamics of the system are governed by the classical Newtonian equation $m_i d^2 r_i / dt^2 = \sum_{j \neq i} F_{ij}$, where m_i and r_i are the mass and position of atom i , respectively, F_{ij} is the pair force between atoms i and j which is calculated as $F_{ij} = -\partial \phi_{ij} / \partial r_{ij}$, where $\phi_{ij} = 4 \cdot \varepsilon \left[\left(\sigma / r_{ij} \right)^{12} - \left(\sigma / r_{ij} \right)^6 \right]$ is the Lennard-Jones (12-6) potential and used to calculate the force between atoms. For argon $\varepsilon = 1.653 \times 10^{-21}$ J is the LJ well depth parameter, $\sigma = 3.406$ Å is referred to as the equilibrium separation parameter, and $r_{ij} = r_i - r_j$. The general idea is to obtain the atomic positions, velocities, etc. at time $t + \delta t$ based on the positions, velocities, and other dynamic information at time t . The equations are solved on a step-by-step basis, and the time interval δt is dependent somehow on the method applied. However, δt is usually much smaller than the typical time taken for an atom to travel its own length. In this calculation a time step of 25 fs is used. The Newtonian equation is solved by applying the Verlet algorithm, of which the Verlet algorithm is widely used due to its numerical stability, convenience, and simplicity, to velocity [42], which is expressed as:

$$r_i(t + \delta t) = r_i(t) + v(t + \delta t / 2) \delta t \quad (2.1a)$$

$$F_{ij}(t + \delta t) = -\frac{\partial \phi_{ij}(t + \delta t)}{\partial r_{ij}} \quad (2.1b)$$

$$v(t + 3\delta t / 2) = v(t + \delta t / 2) + \frac{F_{ij}(t + \delta t)}{m_i} \delta t \quad (2.1c)$$

The interactions between atoms are truncated at a distance of 2.5σ , beyond which the interactions are negligible. This distance is called the cut off distance (r_c) (fig. 2.1). In this work, only the repulsive force is considered between atoms in the ambient gas. The solid and gas atoms share the same molecular mass and repulsive potential for Group 2 studies. For Group 1 studies, the ambient gas shares the same repulsive potential as the target, but has reduced molecular weight. The initial ensemble momentum is subtracted at the beginning of simulation to keep the total momentum zero. Computation of the force between an atom and its neighbors is arranged by the cell structure and linked-list methods [42]. In the linked-list method, each atom is sorted into an appropriate cell based on their positions. In the code, each number can be identified by their index number given in the beginning and is arranged from cell to cell. An array HEAD is used to store the biggest index number within the cell. Another array LIST is used to store the cell index of each atom within a cell, which is the index number of the next atom within the cell in a decreasing sequence. The cell index for the last atom within the cell is zero. For example, as shown in figure 2.1 in cell $(i-1, j)$, the index number for atoms within this cell is 7, 36, 101, 229, 230. In this cell, HEAD is equal to 230 and cell index are LIST(230)=229, LIST(229)=101, LIST(101)=36, LIST(36)=7, LIST(7)=0. In the force calculation, an atom only interacts with its neighbors within the cell

or the cells next to the current cell. This makes the calculation very time efficient.

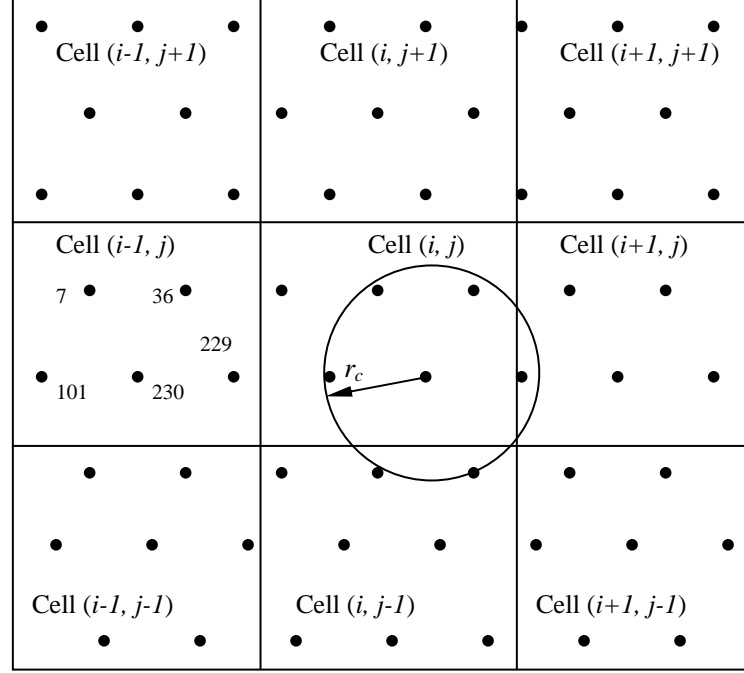


Figure2. 1 Cell structure and linked list in 2-D plate

In the calculation, non-dimensionalized parameters are used, which are listed in Table 2.1. After non-dimensionalization, Eqs. $m_i d^2 r_i / dt^2 = \sum_{j \neq i} F_{ij}$, $\phi_{ij} = 4 \cdot \varepsilon \left[\left(\sigma / r_{ij} \right)^{12} - \left(\sigma / r_{ij} \right)^6 \right]$ and $F_{ij} = -\partial \phi_{ij} / \partial r_{ij}$ become

$$\frac{d^2 r_i^*}{d(t^*)^2} = \sum_{j \neq i} F_{ij}^* \quad (2.2a)$$

$$\phi_{ij}^* = \frac{1}{(r_{ij}^*)^{12}} - \frac{1}{(r_{ij}^*)^6} \quad (2.2b)$$

$$F_{ij}^* = \left(-\frac{12}{(r_{ij}^*)^{14}} + \frac{6}{(r_{ij}^*)^8} \right) \cdot r_{ij}^* \quad (2.2c)$$

Parameters used in the calculation are listed in Table 2.2. During the initialization, as discussed above, the positions and velocities are specified for time 0. On the other hand, from Eq. (2.1c), it is seen that only velocities at half time step are used. Therefore, in order to start the calculation, velocities at $\delta t^* / 2$ are calculated after the initial velocity specification,

$$v^*(t^* + \delta t^* / 2) = v^*(0) + F_{ij}^*(0) \delta t^* / 2 \quad (2.3)$$

where $F_{ij}^*(0)$ is calculated using Eqs. (2.2a-2.2c).

Table 2.1 Non-dimensionalized parameters

Quantity	Equation
Time	$t^* = t / (\sigma \sqrt{m / 4\varepsilon})$
Length	$r^* = r / \sigma$
Mass	$m^* = m / m = 1$
Velocity	$v^* = v / \sqrt{4\varepsilon / m}$
Potential	$\phi^* = \phi / 4\varepsilon$
Force	$F_{ij}^* = F_{ij} / (4\varepsilon / \sigma)$
Temperature	$T^* = k_B T / 4\varepsilon$

The form of Eqs. (2.1a) and (2.1b) is preserved, while Eq. (2.1c) becomes

$$v^*(t^* + 3\delta t^*/2) = v^*(t^* + \delta t^*/2) + F_{ij}^*(t^* + \delta t^*)\delta t^* \quad (2.4)$$

2.2 Parallel computation

Although Linked-list method has already saved this simulation tremendous computing time, to trace a system constitutes over 2 million atoms is still a time-consuming work. To reduce the computational time, the programs are further modified using Message Passing Interface to realize parallel computation. As a result, the computational time for each step is about 7 seconds by employing 4 processors, which is almost 1/4 the time required if only one processor is used for computation. Figure 2.2 illustrates the schematic of the parallel computation. The whole domain is divided evenly into 4 sub-domains in the y direction. Each sub-domain is computed by one processor. At every time step, each processor will do self diagnosis at its right and left boundaries. If one atom moves out of the boundary limit of the present sub-domain, it will be excluded from the present one and passed to its physical neighbor. So each processor will exchange atoms with its neighbors every time step. For the left and right boundaries of the whole domain, periodical boundary conditions are applied to deal with those atoms that may move out of the computational space. This means the atoms excluded from Processor 4 will enter Processor 1. Under this condition, the total number of tracked atoms remains constant. In this simulation, the domain size in the y direction is designed to keep the shock wave movement within the domain as much as possible.

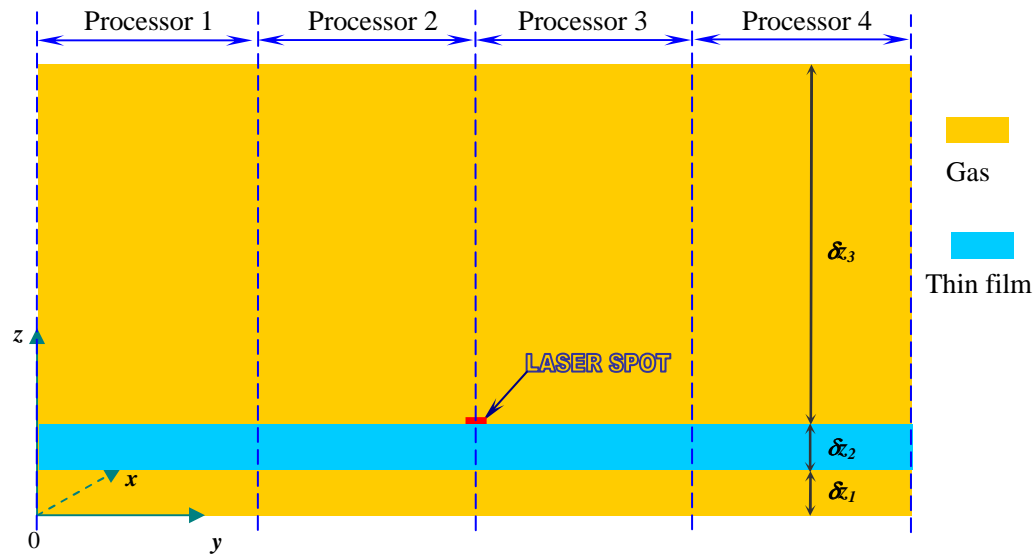


Figure 2. 2 Schematic of the MD configuration for shock wave study and parallel computation (Domain sizes under different conditions are listed in Table 3).

2.3 Laser material interaction

The work done by our laboratory has proved that the physical model used in this work makes the ambient gas very close to the ideal gas situation [24]. This is due to the large spacing among gas atoms and the weak interaction between them. The pressure and sound speed based on the ideal gas model for the simulated cases in this work are summarized in Table 2.3. The density of the ambient gas used in pressure evaluation is calculated using the total number of gas atoms and the gas domain size in our MD simulation.

The laser beam follows the Gaussian distribution in space and time domains

$$I = I_0 \exp\left(-\frac{(r - r_o)^2}{r_g^2}\right) \cdot \exp\left(-\frac{(t - t_o)^2}{t_g^2}\right), \quad (2.5)$$

where I_0 is a laser beam intensity constant, r is the location of the laser beam, r_o the center of the beam, r_g the size constant of the laser spot, t the laser heating time, t_o the peak location of the laser in the time domain, and t_g the characteristic time of the laser pulse width.

Table 2.2 Values of the parameters used in the simulation

Parameter	Value
ε , LJ well depth parameter	1.653×10^{-21} J
σ_e , LJ equilibrium separation	3.406 Å
m , argon atomic mass	66.3×10^{-27} kg
k_B , Boltzmann's constant	1.38×10^{-23} J/K
a , lattice constant	5.414 Å
r_c , cutoff distance	8.515 Å
τ , laser beam absorption depth	10 nm
$\delta\tau$, time step	25 fs
I_o	3.74×10^{12} Wm ⁻²
r_g	2 nm
t_o	10 ps
t_g	3 ps

Table 2.3 Sound speed and pressure under ideal gas assumption

Group	Conditions	Pressure (MPa)	Sound speed (m/s)
1	$\beta = 2, \gamma = 1$	0.217	93
	$\beta = 1, \gamma = 1$	0.217	132
	$\beta = 0.5, \gamma = 1$	0.217	186
	$\beta = 0.25, \gamma = 1$	0.217	263
	$\beta = 0.125, \gamma = 1$	0.217	373
2	$\beta = 1, \gamma = 0.25$	0.0543	132
	$\beta = 1, \gamma = 0.0626$	0.0136	132
	$\beta = 1, \gamma = 0.0157$	0.0034	132

The laser energy transmission in materials obeys the Lambert law $I = -Idz/\tau$, where I is the laser beam intensity, τ the absorption depth, and z the coordinate in the laser incident direction. The absorption depth is dependent on the material and laser wavelength. When conducting the simulation, 10 nm is used as the value of τ . This arbitrary value is chosen to reflect the fact of volume absorption in the material rather than to represent a realistic experimental condition.

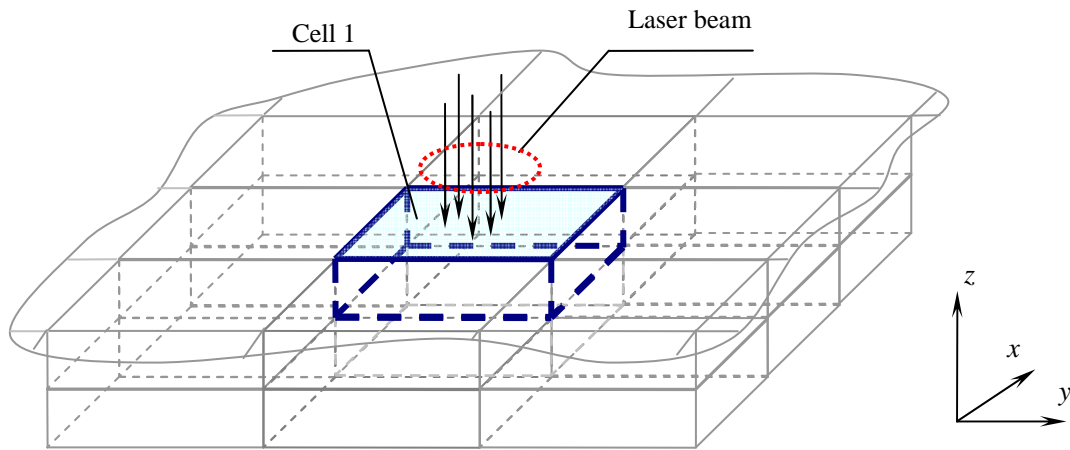


Figure2. 3 Schematic of the laser beam absorption in the material.

Figure 2.3 shows the schematic of the laser beam absorption in the material. The laser energy absorbed by atoms within each time step for Cell 1 is

$$\delta E_1 = E_1 [1 - \exp(\delta z / \tau_1)] \quad (2.6)$$

where δz is the size of cells in the z direction. In MD simulation, δz (cell size) is chosen to be a little larger than the cutoff distance (2.5σ) in order to use the linked-list method. The actual absorption depth in Cell 1 is adjusted as $\tau_1 = \tau \cdot \rho_0 / \rho_1$ with ρ_1 the density of atoms in Cell 1 and ρ_0 the density of argon at 50 K. The incident laser energy on the adjacent cell below Cell 1 will be $E_1 - \delta E_1$, and so on to the next cell. The energy absorption is achieved by scaling the velocity of atoms in each cell. Details were discussed in Wang's previous work [22].

CHAPTER 3: SHOCK WAVE IN LASER-INDUCED NANOMANUFACTURING

As described previously, the dimensions of the domain for each case are 2.707×920.38 (or 900.89×595.54 nm ($x \times y \times z$)) for group 1 and $2.707 \times 900.89 \times 1801.78$ nm for group 2 (listed in Table 3.1). The total number of atoms in the computational domain is also summarized in Table 3.1. The pulsed laser energy is 0.25 fJ ($\text{fJ} = 10^{-15}$ J), and the pulse width is 5 ps full width at half maximum (FWHM) (Table 2.2). For the optical absorption depth used in this work (10 nm), the target material is thick enough to have sound absorption of the laser energy. We have conducted different simulations and found that for thinner target materials (e.g., 20 nm), some of the laser energy will pass through the target. Additionally, the strong recoil pressure in laser ablation will bend thin targets to introduce unrealistic physical phenomena. The size of the target used in this work is chosen to have a large absorption of the laser energy while reducing the computational time as much as possible. Thicker targets (e.g. 60 nm) have been used in our MD modeling of laser-induced surface nanostructuring and no appreciable difference is observed in comparison with the results using films 30 nm thick [43].

Shown in Fig. 3.1 are the snapshots of the simulated systems at different instants. The

blue and red dots represent ambient gas and target atoms, respectively. As mentioned above, the size difference in the z coordinate is due to the construction of the modeled system. And since the area below the film will not be influenced by the shock wave, only the area above the film and the top layer of the film is plotted out in each case. Particularly, for each snapshot in Fig. 3.1, the axis is 50-595 nm in the z direction and 0-900 nm in the y direction.

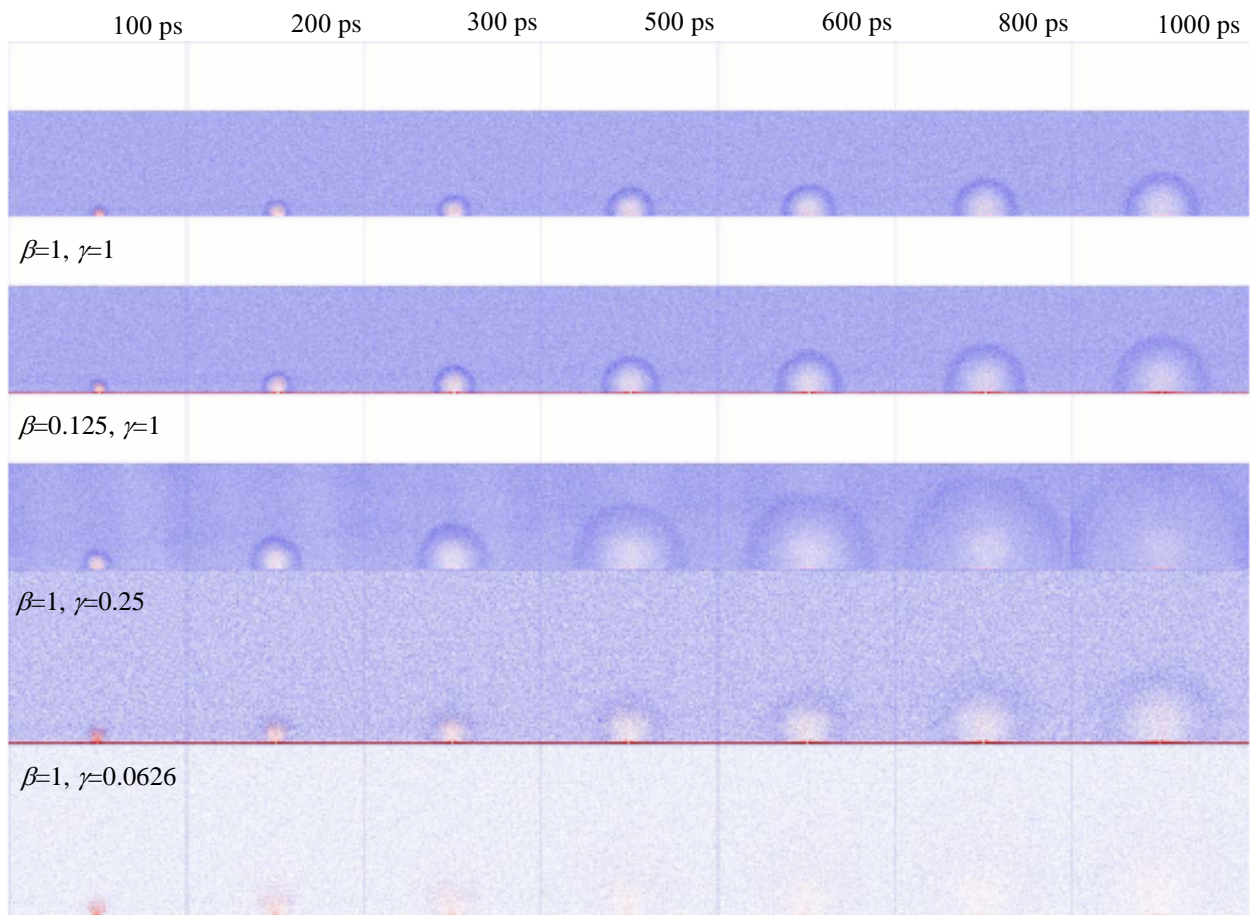


Figure 3. 1 Evolution of atomic positions during shock wave formation and propagation (different cases at different time instants are listed in the column). Each dot in the figure represents an atom. Red dots: target atoms; blue dots: ambient gas atoms. Horizontal coordinate: y coordinate in the simulation (0-900 nm). Vertical coordinate: z coordinate in the simulation (50-595 nm)

Table 3.1 Conditions, domain sizes and total number of atoms for different groups

Group	Conditions	δz_1 (nm)	δz_2 (nm)	δz_3 (nm)	l_x (nm)	l_y (nm)	N
1	$\beta=2, \gamma=1$	21.656	32.484	541.4	2.707	920.38	2,480,960
	$\beta=1, \gamma=1$	21.656	32.484	541.4	2.707	920.38	2,480,960
	$\beta=0.5, \gamma=1$	21.656	32.484	541.4	2.707	920.38	2,480,960
	$\beta=0.25, \gamma=1$	21.656	32.484	541.4	2.707	920.38	2,480,960
	$\beta=0.125, \gamma=1$	21.656	32.484	541.4	2.707	900.89	2,429,440
2	$\beta=1, \gamma=0.25$	34.650	34.650	1732.479	2.707	900.89	2,469,376
	$\beta=1, \gamma=0.0626$	34.650	34.650	1732.479	2.707	900.89	2,214,784
	$\beta=1, \gamma=0.0157$	34.650	34.650	1732.479	2.707	900.89	2,151,136

δz_1 : ambient gas thickness below target film; δz_2 : target film thickness; δz_3 : ambient gas thickness above target film; l_x : domain size in the x direction; l_y : domain size in the y direction; N : total number of atoms within the domain

Figure 3.1 shows the formation and propagation of the shock wave front in space for five typical cases. As reported in literatures, the intensive laser heating causes the material to experience rapid phase change and explosion [18, 22]. The exploded material creates a plume which propagates into the ambient gas. The plume penetrates the ambient gas with a speed exceeding the local sound speed (Table 2.3) that consequently forms a shock wave (Fig 2.4). Because of the energy dissipation, the movement of target atoms will slow down but the gas wave will still exist and push the ambient gas to move [24]. A general trend observed in Fig. 3.1 is that under the same ambient pressure ($\gamma=1$), when the ambient molecular mass is heavier (meaning denser ambient gas and higher β value), the shock wave moves slower, largely due to the strong constraint from the ambience which suppresses the phase explosion

very much. When the pressure of the ambient gas is getting lower (lower pressure and smaller γ value), the strength of the shock wave is weakened, and the shock wave becomes hard to distinguish ($\beta=1$, $\gamma=0.0626$). This is because the lower number density of atoms in the ambient gas leaves significant spacing for the ablated material to penetrate with little scattering. For the lowest pressure case ($\beta=1$, $\gamma=0.0626$), no shock wave is observed. The ablated atoms penetrate into the ambient gas and mix with them.

3.1. Evolution of shockwave front

To investigate the movement of the shock wave front, first the position and speed of ambient gas atoms and target atoms are calculated separately and plotted in space. Figure 3.2 shows the snapshots at 100, 400, and 800 ps for five different ambient gas molecular weights. The black dots and red dots represent the target and gas atoms; the blue and pink lines represent the velocity of ablated target atoms and ambient gas. Only the central part in the y direction with a size about 17 nm (Δy) is used for this calculation. Basically, the velocity here does not represent the speed of shock wave front propagation, but is the mass velocity. As shown in these figures, the movements of both kinds of atoms are faster in lighter gas ambience. Comparison between the case ($\beta=0.125$, $\gamma=1$) and ($\beta=2$, $\gamma=1$) at 100 ps strongly supports this argument. This is because when the ambient gas is lighter, it imposes less constraint on the ejected plume, leading to higher plume velocity. At 400 ps, the speed of

target atoms in case ($\beta=0.5, \gamma=1$) decays faster than case ($\beta=1, \gamma=1$), but the speed of ambient gas is higher than that in ($\beta=1, \gamma=1$). From the figures at 400 ps, it is clear that when a lighter ambient gas is present, the shock wave moves faster. At 800 ps, the wave formed by moving atoms disappears in case ($\beta=0.25, \gamma=1$) and ($\beta=0.125, \gamma=1$). But in case ($\beta=0.5, \gamma=1$), ($\beta=1, \gamma=1$), and ($\beta=2, \gamma=1$), the bulk movements of atoms in the ambient gas are still recognizable, which means the propagation will keep going.

To further investigate the shock wave phenomena, we use three parameters: shock wave front position, propagation velocity and Mach number in attempt to describe the movement of the shock wave front. The shock wave front position is estimated by direct observation of atomic snapshots in the direction normal to the target surface, where a density jump can be observed. The velocity is derived from $v = dz/dt$. The determination of Mach number (M) follows $M=v/v_s$ where v is the velocity of the shock wave front, v_s is the local sound speed, which is determined based on the ideal gas model. For monatomic gases, v_s is calculated using the following formula

$$v_s = \sqrt{\gamma k_B T / m_o}, \text{ with } \gamma = c_p / c_v = (c_v + R) / c_v \text{ and } c_v = 3/2R, \quad (3.1)$$

where γ is the adiabatic index, R the universal gas constant, m_o the atomic mass, and T temperature. Table 2.3 lists the speed of sound calculated in this work.

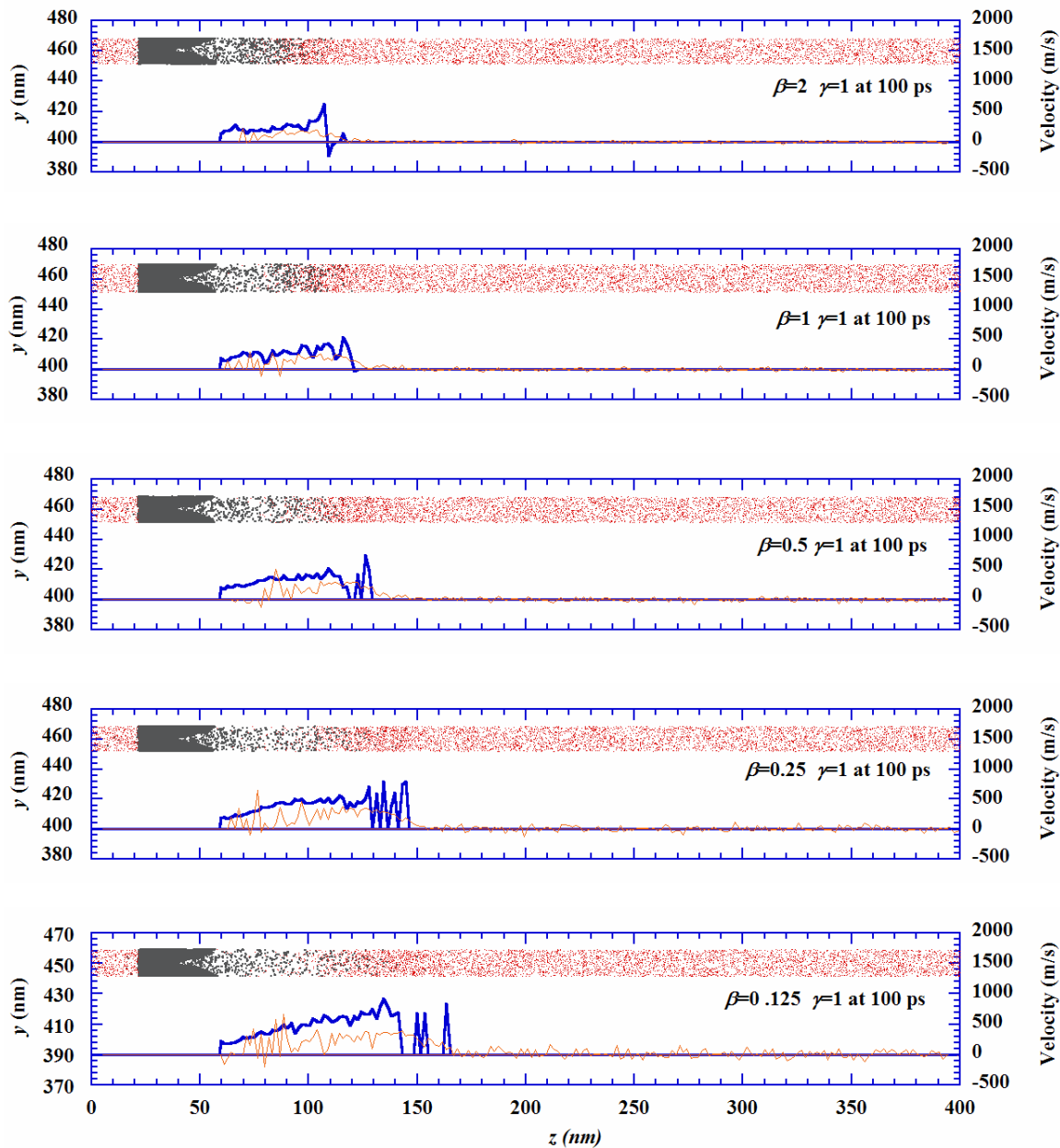


Figure 3. 2 Movements of target atoms and ambient gas atoms (black dots and blue lines represent target atoms and their speed; red dots and pink lines represent ambient gas atoms and their speed).

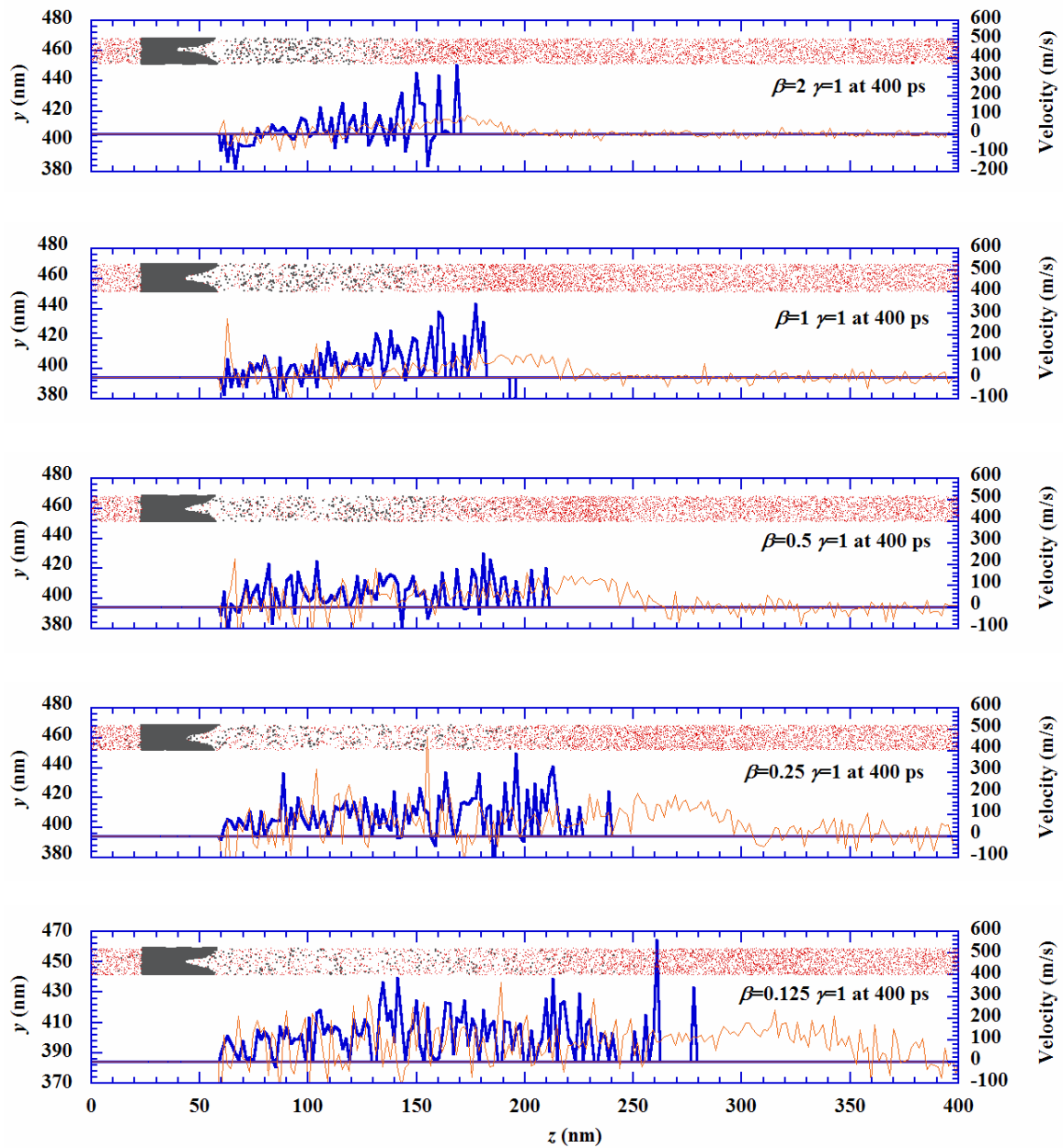


Figure 3.2. (continued).

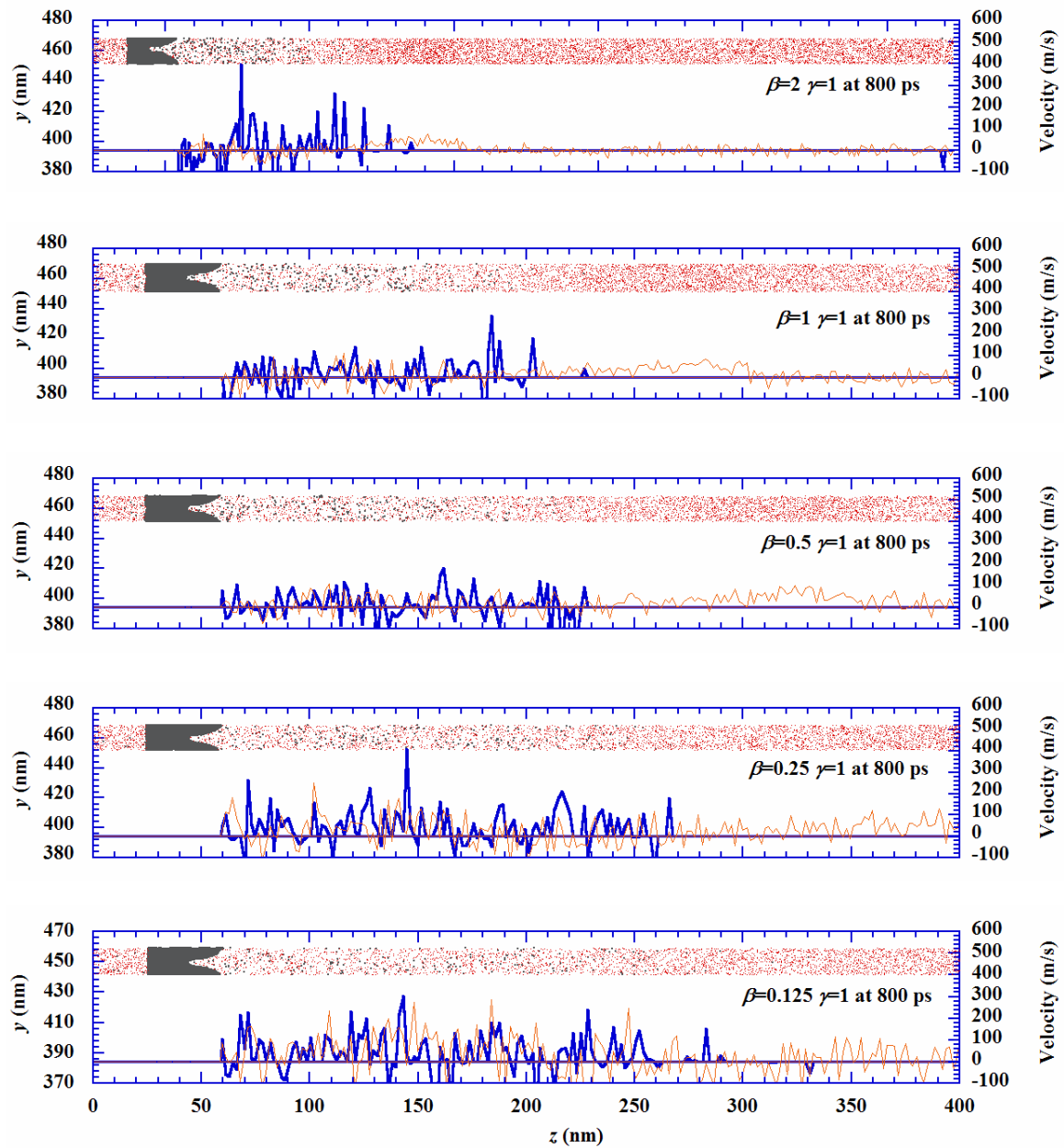


Figure 3.2. (continued).

For some cases, the interface between the shock wave front and the ambience is too vague to distinguish at long times (1 ns). For example, in case ($\beta=0.125 \gamma=1$) the shock wave

front almost disappears at 400 ps. For case ($\beta=2$ $\gamma=1$), from 0 to 30 ps the shock wave front only propagates a very short distance, and is difficult to distinguish. To suppress the statistical uncertainty, the position in this case is recorded starting from 30 ps. Shown in Fig. 3.3 are the shock wave front position and velocity against time. The symbols are the observable front position (MD simulation), and the solid lines are the fitting curve of the position data in Fig. 3.3 (a). It is observed that the molecular mass of the ambient gas has significant impact on the shock wave propagation speed. At the beginning, the front propagates with a speed up to 1200 m/s. But the movement decays quickly as the shock wave front is constrained by the stationary ambient gas. The decay slows down and the shock wave front reaches a relatively steady speed after some time. This time is different for each case from about 250 to 550 ps. For lighter ambient gas, the shock wave front movement can be quite steady after 200 ps ($\beta=0.125$, $\gamma=1$) while for heavier ambient gas, the movement of the shock wave decays till 550 ps. For heavier gas environment, the propagation is sluggish but will last a longer time. The movement in lighter ambience could reach a speed up to 1200 m/s, but does not last long.

The evolution of Mach number under different molecular mass ratios is shown in Fig. 3.4. For the five cases, the ambient pressure is almost the same, around 0.217 MPa. At the early stage of shock wave development, the Mach number is higher in case ($\beta=2$, $\gamma=1$) and ($\beta=1$, $\gamma=1$) followed by case ($\beta=0.5$, $\gamma=1$), ($\beta=0.25$, $\gamma=1$) and ($\beta=0.125$, $\gamma=1$). At the late stage,

the Mach number for all cases becomes almost the same. Although the shock wave front propagates faster in lighter ambient gases, the speed of sound increases, too. This explains why the Mach number differs little among these cases at the late stage of shock wave formation. After about 400 ps, the density jump at the shock wave front in case ($\beta=0.125$, $\gamma=1$) becomes difficult to recognize. The ablated atoms stop moving forward at a distance around 250 nm. The energy of the shock wave then will be dissipated through the form of sound wave.

3.2. Evolution of the interaction zone

Once the shock wave forms, its interaction with the ambient gas is a very important phenomena since such interaction can strongly influence the evolution of the plume and the nanoclusters inside. An interaction zone is defined above the film where the ejected target atoms interact strongly with the ambient gas atoms. In this section how the size of the interaction zone evolves during shock wave propagation is explored. Since the shock wave propagation occurs within a limited space, only the space above the film is considered. In order to exclude the melted target near the film surface, the starting calculation point is 61 nm in the z direction. Assuming an area containing one or both of the target atoms and ambient atoms, the calculation takes the following three situations into consideration: if both the two kinds of atoms have the same amount (number of atoms), this area is deemed as 100% for interaction; if the area contains only one kind of atoms, this area is deemed as 0% interaction; otherwise, the percentage of the area for interaction is dependent on the relative

number of each kind of atoms in the area. To reflect the evolution of the interaction zone, this area is divided into small areas with 10 cells in the z and y directions. Integrating the interacting area over the whole domain of interest, using n_g and n_t to represent the number of ambient gas and target atoms, and A the area, the calculation of total interaction zone area (A_{IZ}) at each time step is

$$A_{IZ} = \int_A \frac{4n_g n_t}{(n_g + n_t)^2} dA . \quad (3.2)$$

dA is calculated as $dy \cdot dz$ where dy and dz are the size of the discrete cell for interaction zone calculation. Selection of size for the discrete cell is critical to obtain physically reasonable results for the interaction zone. The size should be both sensitive and relative stable to reflect the evolution of the interaction zone. If the cell is too small, large noise would be introduced. Results from too large cells cannot give any meaningful insights into the shock wave propagation. Figure 3.5 is the evolution of interaction zone area for different cases.

For different gas environment under the same pressure, the area of the interaction zone increases fast at the beginning, then slows down and reaches a stable value after some time. Here we define a full development time (FDT) to describe this period. It is expected that the interaction zone area will increase when β decreases since the speed of the shock wave is higher for smaller β . For each kind of gas, the FDT increases as β increases. In case ($\beta=2$, $\gamma=1$), it takes about 500 ps for the plume to fully develop and 250 ps for case ($\beta=0.125$, $\gamma=1$). These time instants coincide with the time noticed in Fig. 3.3(b) when the movement of the shock wave fronts reach a relatively steady speed. The flat line after the FDT may suggest that the bulk movement of ejected atoms stops after the FDT. On the other hand, the shock

wave front keeps propagating in the ambient gas. Figure 3.5 shows that for cases of ($\beta=0.125$, $\gamma=1$) and ($\beta=0.25$, $\gamma=1$), there is a slight drop in the interaction zone area at the end of the simulation. This may result from the high speed of ejected target atoms which push the ambient gas atoms to move so fast that some of the atoms exceed the boundary in the z direction. Due to the periodical boundary conditions, the atoms will re-enter the computational domain from the opposite side, constrain the propagation of the shock wave, and reduce the interaction zone area.

For the same ambient gas at different pressures, Fig. 3.5 shows that as γ (pressure) decreases, the interaction zone area increases rapidly. This increasing speed is far higher than the area increasing speed in case ($\beta=1$, $\gamma=1$) where the pressure is much higher. For ($\beta=1$, $\gamma=0.0157$) and ($\beta=1$, $\gamma=0.0626$), the plume propagates in space with little constraint since the atomic spacing in the ambient gas in these cases is very close to, or larger than the size of the laser spot. Therefore, the ablated materials (atoms, clusters) have a good chance to go through the atomic spacing in the ambience with little scattering. For ($\beta=1$, $\gamma=0.25$), the interaction zone area increases much slower than cases of ($\beta=1$, $\gamma=0.0157$) and ($\beta=1$, $\gamma=0.0626$). At 600 ps, the interaction zone area for ($\beta=1$, $\gamma=0.0626$) becomes smaller than that for ($\beta=1$, $\gamma=0.25$). This could be due to the fact that ablated materials moves faster for ($\beta=1$, $\gamma=0.0626$), and they move out of the computational domain and re-enter from the opposite side. Such phenomena slows the mixing process between the ablated material and the ambient gas. The evolution of the interaction zone for the plume and the ambient gas suggests that the plume can affect a larger area in lower ambient pressure or lighter ambient gas, which has been observed in the experiment conducted by Edens *et al.* [44].

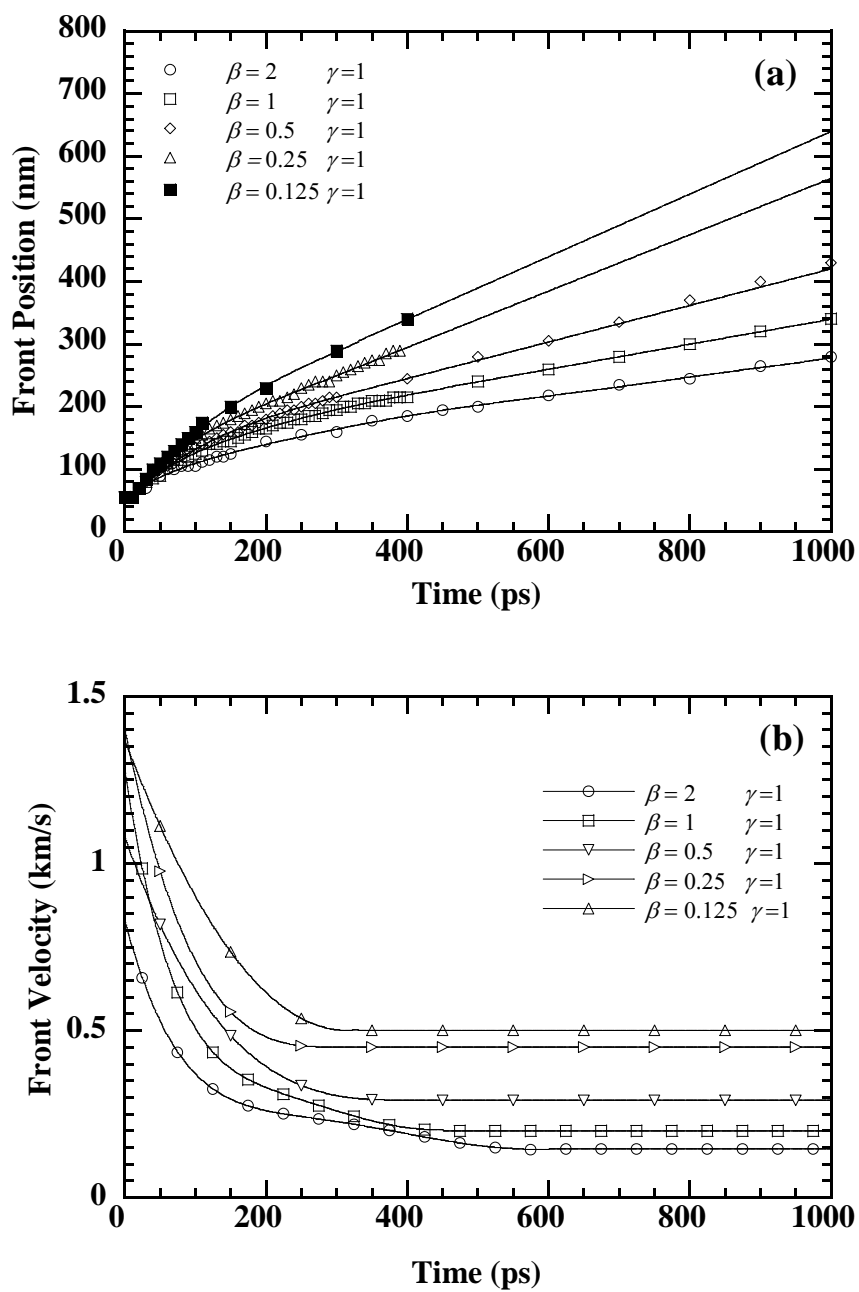


Figure 3.3 Shock wave front positions (a) and velocities (b) in different ambient gases. In figure (a), the solid lines are the fitting curve of the MD data.

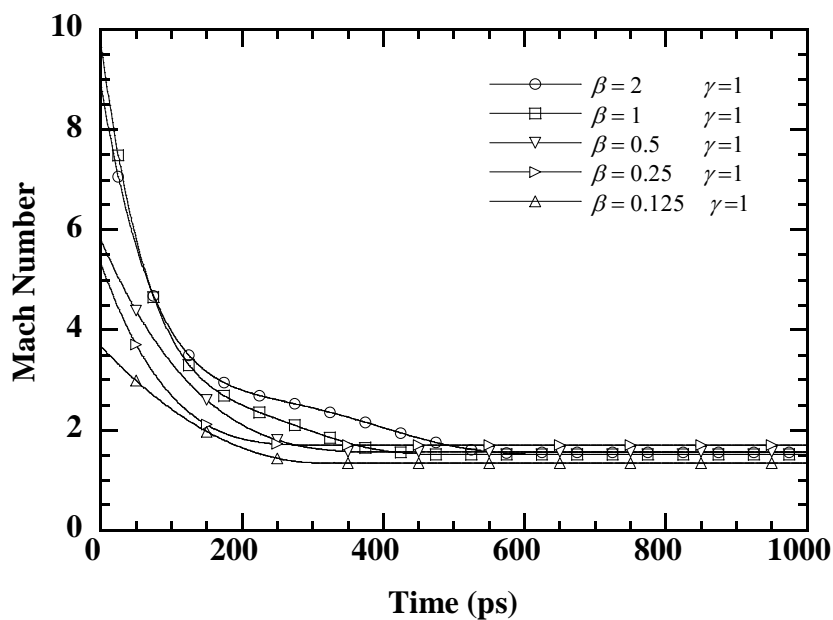


Figure 3. 4 Decay of the Mach number of the shock wave front propagation in different ambient gases.

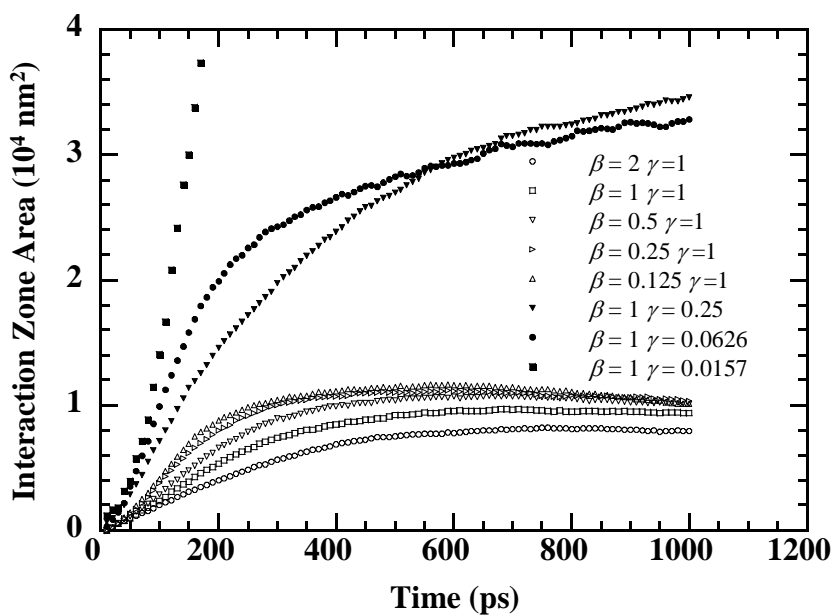


Figure 3. 5 Evolution of the interaction zone area under the influence of different β and γ .

3.3. Energy exchange between plume and ambient gas in the shockwave

During laser ablation, the laser energy will be dissipated in the film in forms of phase change and stress wave, and through shock wave propagating in the ambient gas. Many studies have been conducted with respect to the absorption of laser energy during laser ablation. In this work, the energy exchange between the ablated target atoms and the ambient gas atoms is explored in attempt to study the effect of ambient gas on the energy exchange. The total kinetic energy of the ejected atoms and kinetic energy change of the ambient gas atoms are calculated separately for different β and γ . The results are plotted in Fig. 3.6. Under the same ambient pressure, it can be seen [Fig. 3.6 (a)] that the energy increase in different ambient gases is about 2×10^{-17} J, regardless of the molecular mass. The energy of the ablated target atoms decreases as β increases during the early stage but reaches almost the same level after a while [Fig. 3.6 (a)].

In the same gas ambience, the density jump at the shock wave front exists for the case ($\beta=1$, $\gamma=1$) but becomes invisible for ($\beta=1$, $\gamma=0.0626$) (Fig. 3.1). The curves of energy change for the ambient atoms [Fig. 3.6 (b)] become less steep as γ decreases. For case ($\beta=1$, $\gamma=0.0157$), the energy increase of the ambient gas has become almost linear with time. Under lower ambient pressure, it takes a longer time for the ambient gas to reach a steady energy state due to the rare scattering between the ablated target atoms and ambient atoms. Weaker energy increase in the ambient gas is attributed to the fact that no shock wave is observed in case ($\beta=1$, $\gamma=0.0157$). The ablated atoms and the ambient gas atoms have very little interaction and energy exchange due to the large atomic spacing of the ambient atoms. The energy

increase of the ambient gas is faster and higher in higher pressure environment. It is conclusive from Fig. 3.6(b) that that more energy goes into the plume instead of the ambient gas in lower pressure gas environment.

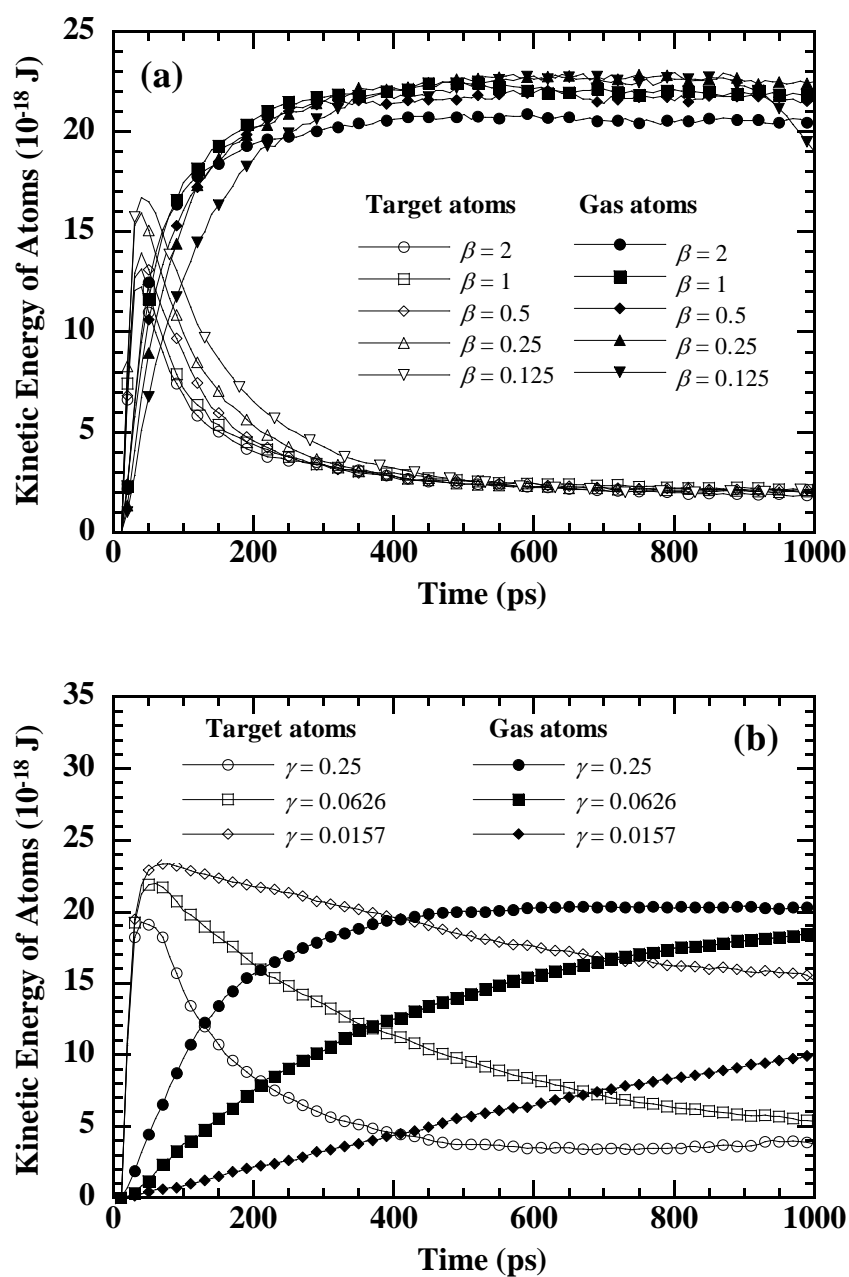


Figure 3. 6 Kinetic energy of ejected atoms and kinetic energy change of ambient gas atoms: (a) under different molecular mass ratios ($\gamma = 1$); (b) under different gas pressures ($\beta = 1$).

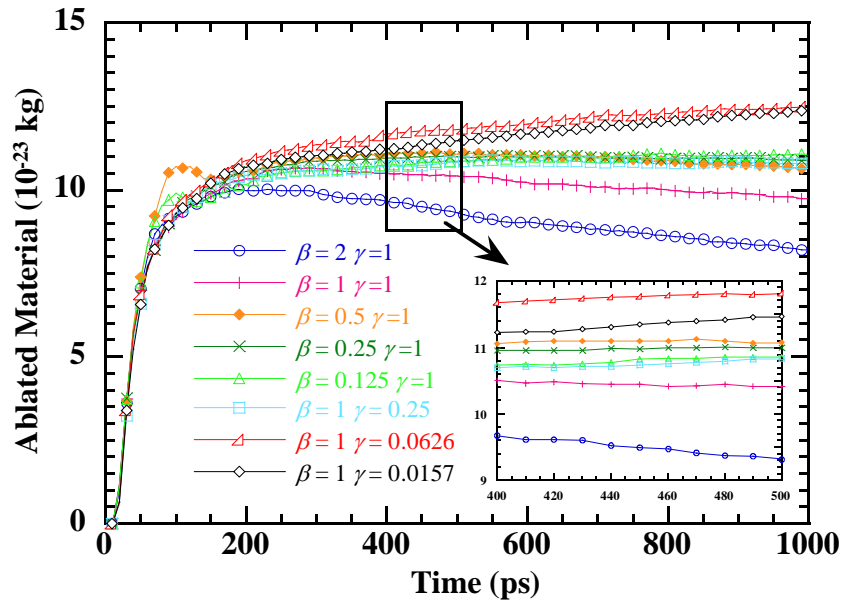


Figure 3. 7 Material ablated under the influence of different β and γ .

According to the calculation, the higher ablation rate and lower energy exchange between the ejected target atoms and the ambient gas atoms can be a reason for the above phenomena. By summing up the ablated target atoms in a designated area, the mass of ablated material is calculated and shown in Fig. 3.7. The results show that less ablated material is present in heavier ambient gases. For $(\beta=2, \gamma=1)$ and $(\beta=1, \gamma=1)$, there is an obvious decay in the material ablation after the peak value. From the snapshots in Fig. 3.1 it is seen that the plume under these conditions is still within the domain, which indicates no atoms flying out of the boundary. Therefore the reason for the ablation decay with time can be attributed to the fact that some of the ejected atoms might be bounced back to the surface by the ambient gas. Such phenomena has been observed in our on-going large-scale one-dimensional shock wave modeling. An extreme extension would be that when the molecular mass of ambient gas is infinitely large, some ejected target atoms will penetrate the

ambient gas while others will hit the ambient gas and be reflected back. This will definitely give rise to the late stage ablation decay. In the other 3 lighter ambient gases, although the movement of ejected atoms is slowed down by the environment atoms, the bulk movement does not change direction. As a consequence, the material ablation in $(\beta=0.5, \gamma=1)$, $(\beta=0.25, \gamma=1)$, and $(\beta=0.125, \gamma=1)$ are higher than in $(\beta=2, \gamma=1)$ and $(\beta=1, \gamma=1)$. Under the influence of different γ , it is observed when the pressure is lower (smaller γ), more material will be ablated out due to the less constraint from the ambience. The ablated material is already very close to the ablation limit in vacuum for case $(\beta=1, \gamma=0.0626)$ and $(\beta=1, \gamma=0.0157)$, so in Fig. 3.7 the difference between these two curves is very close (~5% difference).

Mendes and Vilar experimentally investigated the influence of ambient gas on the ablation rate at large scales [45]. The material they used is $\text{Al}_2\text{O}_3\text{-TiC}$ ceramic whose average molecular weight is calculated as 84.3 g/mol. Their study showed that comparing with the ablation rate at 1 bar in Kr $(\beta=1, \gamma=1)$, the ablation rate increased 21.7% in Ar $(\beta=0.48, \gamma=1)$ and 65.2% in Ne $(\beta=0.24, \gamma=1)$ [45]. In this work, the ablation rate increase with respect to the case $(\beta=1, \gamma=1)$ is 11.0% for case $(\beta=0.5, \gamma=1)$ and 11.3% for case $(\beta=0.25, \gamma=1)$ at 2.17 bar. In Kr ambient gas, comparing with the ablation rate at 1 bar, the ablation rate increases 58.3% at 0.25 bar $(\gamma=0.25)$, 75.0% at 0.0626 bar $(\gamma=0.0626)$, and 83.3% at 0.0157 bar $(\gamma=0.0157)$. The ablation rate calculated in this work, comparing with case $(\beta=1, \gamma=1)$, increases 10.8% for case $(\beta=1, \gamma=0.25)$, 12.5% for case $(\beta=1, \gamma=0.0626)$, and 12.4% for case $(\beta=1, \gamma=0.0157)$. The difference between the experiment and MD simulation about the effect of the molecular weight and ambient pressure is probably due to the laser ablation conditions.

The MD simulation of this work is focused on nanoscale (4 nm diameter at e^{-1}) surface laser ablation using a picosecond laser pulse (5 ps FWHM) while the experiment reported in reference [45] is for nanosecond laser ablation (30 ns FWHM) with a laser spot of 250 μm . Nevertheless, both the experiment and MD simulation indicate the same trend for the effect of the molecular weight and pressure of the ambient gas.

3.4. Conclusion

In this chapter, quasi three dimensional systems with over 2 million atoms were simulated using parallel MD simulation. Detailed studies were carried out about the shock wave front and Mach numbers, evolution of plume and ambient gas interaction zone, and energy exchange between the ambient gas and plume. The plume affected a larger area under lower ambient pressure or lighter ambient gas, while the strength of the shock wave front was weaker since the diameter of the plume was larger. It was observed with the same ambient pressure and laser fluence, the ablated material will feature the same kinetic energy at the late stage regardless of the molecular weight of the ambient gas. The same conclusion holds for the energy increase of the ambient gas as well. When the ambient pressure was reduced, more kinetic energy was carried out by the ablated material while less energy was transferred to the ambient gas. By studying the ablation change with time, it was observed that when a heavier ambient gas was present, the ablated material could be bounced back by the ambient atoms.

CHAPTER 4: EXPERIMENTAL DETAIL FOR STUDYING NANOSCALE THERMAL TRANSPORT

4.1 Sample preparation

Highly ordered TiO₂ nanotube arrays are grown on a Ti foil using a modified procedure.[25,47,48] Briefly, Ti foil (Sigma-Aldrich; 250 μm thick, 99% purity) is first degreased by ultrasonication for 30 minutes in a mixture of acetone, methanol, and methylene chloride, followed by a thorough rinse with DI water and blow drying with N₂ gas. Ethylene glycol (Fisher Scientific) is used as the electrolyte. A small amount of ammonium fluoride (Sigma-Aldrich) is added into the ethylene glycol electrolyte. All chemicals and materials in the experiment are used as received without further purification. Electrochemical anodization of Ti foil is carried out in a two-electrode cell at room temperature using a power source EC570-90 (Thermo Electron Corporation), in which a platinum foil is used as the counter electrode. Anodization is conducted at a constant potential of 60 V for a period of time until a desired thickness is reached (Sample 1 is obtained after anodization for 4 hours; Sample 2 is obtained after anodization for 60 hours). After anodization the Ti foil with the TiO₂ nanotubes is thoroughly washed with a large amount of DI water and methanol, and dried by N₂ gas flow. Freshly made TiO₂ nanotube arrays are amorphous covered with a thin

layer of TiO₂ nanowires (shown in Fig. 4.1).^{1,18} In this work, a thin layer of gold film is sputtering deposited on top of the as-prepared TiO₂ nanotube arrays, where it covers the thin layer of TiO₂ nanowires. This gold coating layer (about 200 nm thick) is used in the PT experiment to absorb the laser energy, and is used as the heater and thermal sensor in the TET experiment as detailed below.

Figure 4.1 (a) shows the schematic structure of the sample. From the top to bottom, the layers shown are gold coating, TiO₂ nanowires, free amorphous TiO₂ nanotubes, and Ti substrate. The TiO₂ nanotubes are fabricated on a Ti substrate. For the TET measurement, the TiO₂ nanotube arrays are taken off the Ti substrate to make them free-standing. For the sample measured using the PT technique, the thickness of these layers are 200 nm, 100 nm, 29.2 μm , and 250 μm , respectively.

4.2 Experiment principles

First of all, the density (ρ_{eff}) and thermal conductivity (k_p) of the amorphous TiO₂ nanotube arrays (Sample 1) are characterized along the tube direction using the PT technique. Sample 2 (140 μm thick) is too thick for the PT experiment. Therefore, Sample 1 is used to study the heat transfer along the tube axial direction. For studying the heat transfer in the cross-tube direction using the TET technique, free-standing TiO₂ nanotube array from Sample 1 is too thin and easily breaks when it is suspended between electrodes. Therefore,

Sample 2 is used for studying the heat transfer in the cross-tube direction. These two samples are fabricated using the same technique under the exact same experimental conditions.

Therefore, they are expected to have the same thermophysical properties and density. The characterized properties using Sample 1 will be used to obtain the real thermal conductivity of the fabricated amorphous TiO₂ nanotube. As shown in Fig. 4.1(b), an infrared laser beam with wavelength of 809 nm is used to periodically irradiate the sample surface, where the gold coating absorbs the laser energy and heats the layers underneath. Such laser heating will lead to a periodical temperature variation at the surface of the gold layer. This temperature variation is strongly dependent on the thermal transport in the TiO₂ nanotube arrays. The surface temperature variation is measured by sensing the thermal emission from the heating area using an infrared detector. The phase shift ($\Delta\phi$) of the surface temperature variation is measured over a frequency (f) range. This frequency range is carefully selected to ensure that the thermal diffusion depth within one heating period is much smaller than the heating spot. Consequently, the heat transfer within each heating period can be treated as one dimensional along the thickness direction [41]. Then trial values of the density and thermal conductivity of the TiO₂ nanotube arrays are used to fit the measured $\Delta\phi\sim f$ curve. The trial values giving the best fit (least square) of the experimental data are taken as the properties of the material. More details about the PT technique, including experimental setup and system calibration can be found in another work by our group [41]. In our PT measurement, the laser heating spot on the sample surface is about $0.7\times 1.4\text{ mm}^2$.

To fit the density and thermal conductivity of the as-prepared TiO₂ nanotube arrays in the PT experiment, its specific heat (c_p) is needed. Dames *et al.* [49] found that the specific heat of TiO₂ nanotubes approaches the bulk value as temperature increased from 1 to 100 K. So assuming that the specific heat of TiO₂ nanotube arrays is close to the bulk value at the experiment temperature (room temperature), from experimental results by Marton *et al.*[50] (volume-based specific heat capacity of bulk amorphous TiO₂: $2.84 \times 10^6 \text{ J} \cdot \text{m}^{-3} \cdot \text{K}^{-1}$) and Lee and Cahill [22] (density of amorphous TiO₂, $\rho_{\text{bulk}}: 3.9 \text{ g/cm}^3$), the specific heat of TiO₂ nanotube is calculated as $7.28 \text{ J} \cdot \text{kg}^{-1} \cdot \text{K}^{-1}$ and is used in our data processing.

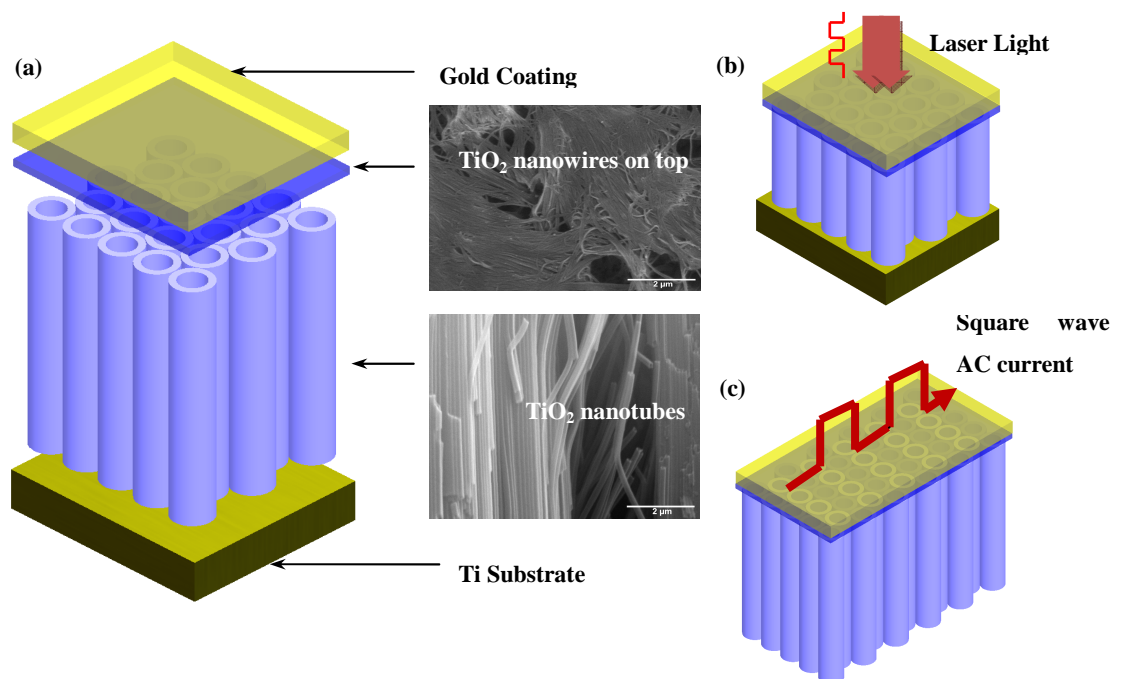


Figure 4. 1 Schematic structure of the TiO₂ nanotube arrays. (a) General structure for TiO₂ nanotubes fabricated on Ti substrate. From top to bottom, the layers are gold coating, TiO₂ nanowires, TiO₂ nanotubes, and Ti substrate; (b) Sample 1 for the PT experiment; (c) Freestanding TiO₂ nanotube arrays sample for TET experiment. The figures are not to scale.

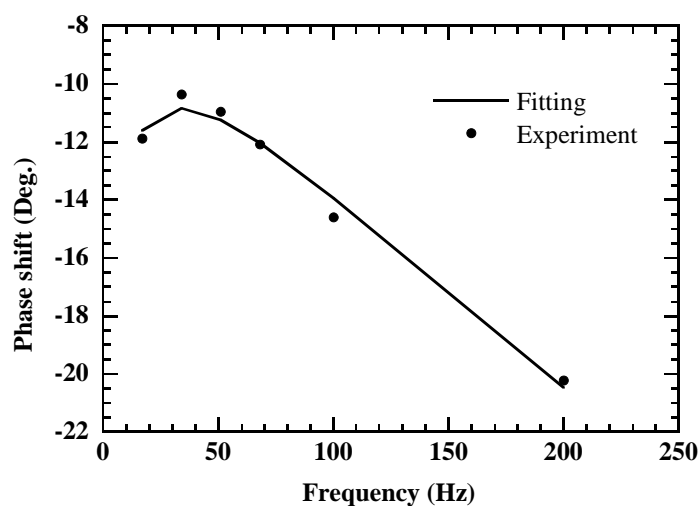


Figure 4. 2 The measured phase shift of surface temperature variation in the PT experiment versus the fitting results for the TiO₂ nanotube arrays (Sample 1: 29.2 μm thick).

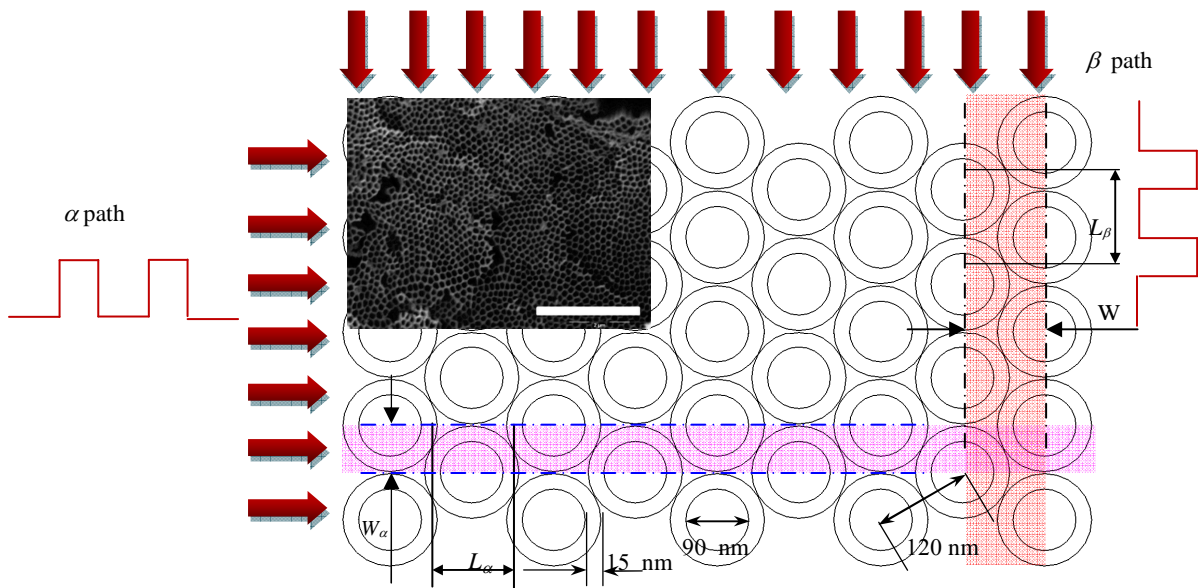


Figure 4.3 Schematic of the heat flow direction along the cross-tube direction. The inset is the SEM image of the top view of TiO₂ nanotube arrays from work done by Jun's *et.al.*¹ L_α and L_β are the calculation units in α and β paths. W_α and W_β are the width of the two paths.

CHAPTER 5: NANOSCALE THERMAL TRANSPORT IN TiO₂ NANOTUBE ARRAYS

Shown in Fig. 4.2 is the experimental result and the fitting curve for the phase shift. The fitted density and thermal conductivity are 0.631 g/cm³ and 0.617 W/K·m, respectively. The thermal conductivity measured here is in fact an effective value which includes the effect of the spacing between and within the nanotubes. The real thermal conductivity of the material can be found by considering the porosity of the TiO₂ nanotube arrays. According to the model proposed by Zhu *et al.*[31], the theoretical porosity of the as-prepared sample is 60% based on the structure shown in Fig.4.3. This theoretical prediction is calculated using inner pore diameter, average wall thickness and center to center pore distance of 90 nm, 15 nm and 120 nm, respectively. However, based on the measured density using our PT technique (0.631 g/cm³), the porosity of the TiO₂ nanotube array is found as $(1-\rho_{\text{eff}}/\rho_{\text{bulk}})=83.8\%$. The difference between the two values indicates high porosity/spacing among nanotubes. The above theoretical porosity (60%) is based on an ideal structure as shown in Fig.4.3. For real TiO₂ nanotube arrays, the nanotubes cannot be that highly compacted. This will make the porosity level higher. SEM images of TiO₂ nanotube arrays in literatures [27,31,32] showed that the average pole distance is larger than the tube outside

diameter, indicating loose contact among nanotubes. Additionally, defects in the nanotubes also will give contribution to the reduced density reported in this work. Based on our measured density, the real thermal conductivity (k) of TiO₂ nanotubes in this work is calculated as $k = k_p / (\rho_{eff} / \rho_{bulk}) = 3.82 \text{ W/K}\cdot\text{m}$. This real thermal conductivity calculation is physically reasonable considering the fact that our measured effective thermal conductivity k_p is for heat transfer along the tube axial direction. Highly ordered orientation exists in this direction as shown in Fig. 4.1(a). Since there are few references available to compare with for the thermal properties of TiO₂ nanotube arrays, our result is compared with the work done on amorphous TiO₂ thin films by Cahill and Allen [39]. In their work, the thermal conductivity at 300 K increased from 1.0 W/K·m to 1.6 W/K·m as the porosity decreased from 12±3% to 4±3%. The lower thermal conductivity in their work is probably due to the existence of nanopores in the film.

As discussed above, although there is no thermal contact resistance along the tube axial direction, it does exist in the cross-tube direction between the tubes. This may lead to the reduction of effective thermal conductivity in the cross-tube direction and cause the material to appear anisotropic. To investigate the thermal conductivity in the cross-tube direction, the TET technique developed in our group by Guo *et al.* [40] is employed to measure Sample 2 which is comprised of highly-ordered freestanding TiO₂ nanotubes (140 μm long) as shown in Fig. 4.1(c). The TET technique overcomes the drawbacks of the

3 ω [39] method and optical-heating-electrical-thermal-sensing (OHETS) technique [52], and is capable of conducting the thermal diffusivity measurement for micro/nanoscale wires/tubes with significantly reduced experiment time and highly improved measurement accuracy [40]. In this technique, the sample is suspended between two electrodes. A square wave AC current [as shown in Fig. 4.1(c)] is applied to the sample to induce a periodical electric heating. The temperature evolution of the sample is tightly related to the heat transfer along the sample. And it will cause a variation of the electric resistance of the sample. By measuring variation of the voltage over the sample, the temperature evolution of the sample can be sensed. Consequently, the thermal diffusivity of the sample can be obtained by fitting the temperature change curve against time. Because TiO₂ nanotube is a semiconducting material, a thin layer of gold has to be deposited on the surface to make it electrically conductive. The coated layer is thin enough comparing to the thickness of the sample. Thus the thermal effect caused by the coated layer can be subtracted by using the Lorenz number without increasing the uncertainty [40]. The thermal diffusivity (α) of sample 2 is calculated by equation (5.1) as below [40]:

$$\alpha = \alpha_e - \frac{L_{Lorenz} TL}{RA_w \rho_{eff} C_p} \quad (5.1)$$

where α_e is the measured thermal diffusivity, L_{Lorenz} ($=2.36 \times 10^{-8} \text{ W}\Omega\text{K}^{-2}$) is the Lorenz number for Au at 300 K, T is room temperature (300 K), L is the sample length, R is the measured resistance of the sample, and A_w is the cross-sectional area of the sample, which is

calculated as $140 \mu\text{m} \times W$, where W is width of the sample.

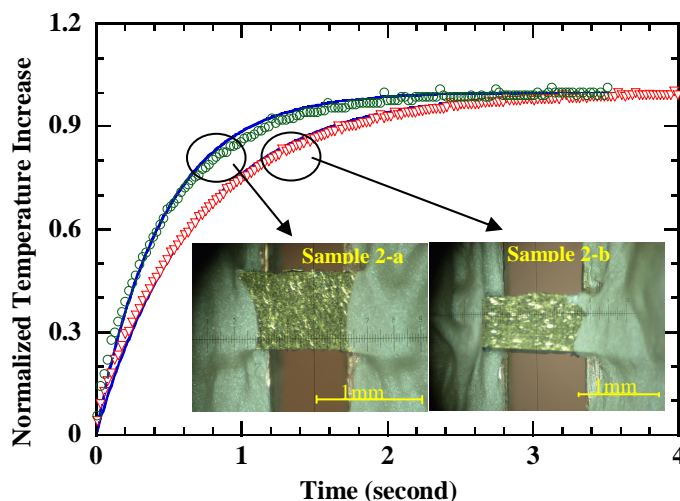


Figure 5. 1 Normalized temperature increase versus the fitting results for the TiO_2 nanotube arrays in the cross-tube direction, measured by TET experiments. The solid lines are the theoretical values for each sample. The circles are the experimental data measured for sample 2-a and the triangles are the experimental data for sample 2-b. The insets are the sample pictures under microscope.

Before the experiment is conducted, the TiO_2 nanotube arrays for sample 2 are removed from the Ti substrate by ultrasonication [Fig. 4.1(c)]. Unlike the PT experiment, only a small piece is needed in the TET experiment. Figure 4 shows the pictures of two tested samples cut off from sample 2 and connected between two electrodes. sample 2-a has a dimension about $1.132 \text{ mm} \times 0.693 \text{ mm}$ and sample 2-b $1.470 \text{ mm} \times 0.615 \text{ mm}$. Sample 2-a is coated with a 260 nm thick Au film on the tube bottom side, and sample 2-b is coated with a 200 nm thick Au film on both the tube bottom side and the surface of the nanowires layer. After coating, each sample is suspended between two copper electrodes and glued with silver

paste.

The normalized temperature increase against time and the theoretical fittings for sample 2-a and sample 2-b are shown in Fig. 5.1. For sample 2-a, the effective thermal diffusivity is found to be $2.23 \times 10^{-7} \text{ m}^2/\text{s}$. Based on the density measured from the PT experiment and specific heat mentioned above, the effective thermal conductivity (k_{\perp}) of the amorphous TiO_2 nanotube arrays in the cross-tube direction is calculated as $0.102 \text{ W/K}\cdot\text{m}$. For sample 2-b, the effective thermal diffusivity and k_{\perp} are $1.67 \times 10^{-7} \text{ m}^2/\text{s}$ and $0.077 \text{ W/K}\cdot\text{m}$, respectively. These values are significantly smaller than the one in the length direction ($0.617 \text{ W/K}\cdot\text{m}$). Since the TiO_2 is amorphous in this work, for the tube wall itself, the thermal conductivity is expected to be isotropic. The anisotropic effective thermal conductivity of the TiO_2 nanotube arrays is due to the anisotropic structure of the array itself. Based on the measured k_{\perp} , one very important property: the thermal contact resistance (R_{tc}) between the TiO_2 nanotubes can be calculated.

For the tube array structure shown in Fig.4.3, we choose two main paths: α and β for the thermal contact resistance analysis since the real heat transfer direction in the TET experiment is not exactly known. From the effective thermal resistance (R_{eff}) and the thermal resistance along the tube wall (R), the thermal contact resistance between the tubes along the two paths can be expressed as:

$$R_{tc,\alpha} = R_{eff,\alpha} / N_{\alpha} - 2R \quad (5.2)$$

$$R_{tc,\beta} = 1.5R_{eff,\beta} / N_{\beta} - 2R \quad (5.3)$$

where $R_{eff} = L/(k_{\perp}hW)$ is the effective thermal resistance of a selected region shown in Fig.4.3 with h the array thickness, $W=W_{\alpha}$ or W_{β} is the sample width shown in Fig.4.3. $R_{eff,\alpha}$ and $R_{eff,\beta}$ are calculated from the measured thermal conductivity of the TiO₂ nanotube arrays with respect to different path width, R is the heat transfer resistance along the tube wall in the cross-tube direction for 60 degrees: $R=r_0\pi/(3kh\delta r)$ with r_0 the mid-point radius of the tube wall and δr the wall thickness, R_{tc} is the contact resistance between two tubes, $N_{\alpha} (=L/L_{\alpha})$ and $N_{\beta} (=L/L_{\beta})$ are the numbers of the calculation unit in the two paths. The calculation shows that the thermal contact resistance between two nanotubes of unit length has the same value using the both path analysis, which is 15.1 for sample 2-a and 20.6 K·m/W for sample 2-b. The difference between the two values may come from the experimental uncertainty and the structure variation. The side view of TiO₂ nanotube arrays in Fig. 4.1(a) shows that the structures from different part of the sample may vary due to the interior defect. In our TET experiment, it is found that the sample is very easy to break when it is connected between two electrodes. This is largely due to the loose contact between TiO₂ nanotubes. Longer (in cross-tube direction) samples are easier to break due to the large stretching force inside induced by connection. This stretching force makes the contact worse among nanotubes, and gives rise to the lower thermal diffusivity (higher thermal contact resistance) for Sample 2-b in comparison with Sample 2-a.

In conclusion, the thermal diffusivity of TiO₂ nanotube arrays in both the tube length and cross-tube directions was measured. Strong anisotropic effective thermal conductivity was observed in our work: 0.617 W/K·m along the tube length direction and 0.077~0.102 W/K·m in the cross-tube direction. Using the PT technique, the density of TiO₂ nanotube arrays was also characterized. Although from the top view of the TiO₂ nanotube arrays, the density of the as-prepared sample was geometrically estimated as 1.56 g/cm³, the actual density is much lower (0.639 g/cm³) due to the loose contact between the tubes. Defects in the nanotubes will also give contribution to the reduced density. The thermal contact resistance between TiO₂ nanotubes was characterized by utilizing both the PT method and TET technique. For the as-prepared samples, the unit length thermal contact resistance 15.1 and 20.6 K·m /W for the two measured samples.

CHAPTER 6: FUTURE WORK

The present work has been concentrated on two areas: MD simulation of laser-induced shock wave during the laser-assisted nanostructuring (Chapter 2-3) and the laser assisted study of nanoscale thermal transport (Chapter 4-5).

In the MD simulation of laser-induced shock wave during the laser-assisted nanostructuring, key interest has been focused on the interaction between the plume and the ambient gas. The evolution and Mach number of the shock wave front, plume and ambient gas interaction zone, and energy exchange between them have been investigated and conclusion has been drawn. It should be mentioned that these conclusions are based on the same laser pulse energy excitation and absorption length. These factors may also have influence on the propagation of the laser-induced shock wave. As an important application of laser assisted nanostructuring techniques, the laser assisted redeposition can also be investigated using MD simulation.

In the laser assisted study of nanoscale thermal transportation, thermal physical properties of amorphous TiO₂ nanotube arrays have been investigated combining the PT and TET techniques. The tested samples are prepared under the same condition. According to literatures on the fabrication of TiO₂ nanotube arrays, TiO₂ nanotube arrays can be fabricated using different techniques and the average tube wall thickness, pore distance, diameter and the tube length can be controlled by varying the fabrication conditions. The difference using

different techniques is obvious under SEM [27, 31-32] thus the variation of thermal physical properties using different fabricating techniques can be a future interest. The size effect of TiO₂ nanotube arrays is also an interest in the future. Although anatase does not exist in bulk materials, it is observed in nanostructures [1]. Therefore, following this work, the anisotropic thermal transport for anatase nanotube arrays can be further investigated.

REFERENCES

- [1]. Kohler M and Freitzsche W 2004 *Nanotechnology* (WILEY-VCH Verlag GmbH&Co. KGaA).
- [2]. Lu Y F, Hu B, Mai Z H, Wang W J, Chim W K and Chong T C 2001 *Jpn. J. Appl. Phys.* **40** 4395-8.
- [3]. Jersch J, Demming F and Dickmann K 1997 *Appl. Phys. A* **64** 29-32.
- [4]. Lu Y F, Mai Z H, Zheng Y W and Song W D 2000 *Appl. Phys. Lett.* **76** 1200-2.
- [5]. Jersch J and Dickmann K 1996 *Appl. Phys. Lett.* **68** 868-70.
- [6]. Jersch J, Demming F, Hildenhagen L J and Dickmann K 1998 *Appl. Phys. A* **66** 29-34.
- [7]. Lu Y F, Mai Z H, Qiu G and Chim W K 1999 *Appl. Phys. Lett.* **75** 2359-61.
- [8]. Hu B, Lu Y F, Mai Z H, Song W D and Chim W K 2000 *First International Symposium on Laser Precision Microfabrication, Omiya, Saitama, Japan*, pp. 232.
- [9]. Mai Z H, Lu Y F, Huang S M, Chim W K and Pan J S 2000 *J. Vac. Sci. Technol. B* **18** 1853-7.
- [10]. Mai Z H, Lu Y F, Song W D, Chim W K 2000 *Appl. Surface Sci.* **360** 154-155.
- [11]. Saiki T and Narita Y 2002 *JSAP Int.* **5** 22-9.
- [12]. Jin E X and Xu X F 2005 *J. Quant. Spectrosc. Radiat. Transfer* **93** 163-73.
- [13]. Wang L, Jin E X, Uppuluri S M and Xu X F 2006 *Opt. Express* **14** 9902.

- [14]. Fang N, Lee H, Sun C and Zhang X 2005 *Science* **308** 534-7.
- [15]. Lu Y F, Mai Z H and Chim W K 1999 *Jpn. J. Appl. Phys.* **38** 5910-5.
- [16]. Chimmalgi A., Choi T and Grigoropoulos C P 2002 *ASME International Mechanical Engineering Congress and Exposition, New Orleans, LA*, pp. 291–5.
- [17]. Huang S M, Hong M H, Lu Y F, Lukyanchuk B S, Song W D and Chong T C 2002 *J. Appl. Phys.* **91** 3268-74.
- [18]. Porneala C and Willis D A 2006 *Appl. Phys. Lett.* **89** 211121-3.
- [19]. Zhang Z and Gogos G 2004 *Phys. Rev. B* **69**, 235403-9.
- [20]. Jeong S H, Greif R and Russo R E 1999 *J. Phys. D: Appl. Phys.* **32** 2578-85.
- [21]. Kohen D and Martens C C 1999 *J. Chem. Phys.* **111** 4343-50.
- [22]. Wang X 2005 *J. Phys. D: Appl. Phys.* **38** 1805.
- [23]. Wang X and Lu Y 2005 *J. Appl. Phys.* **98** 114304-10.
- [24]. Feng X and Wang X 2007 *Phys. Lett. A* **369** 323–7.
- [25]. Wang J and Lin Z Q 2008 *Chem. Mater.* **20**, 1257.
- [26]. Perez-Blanco J M and Barber G D 2008 *Sol. Energy Mater. Sol. Cells* **92**, 997.
- [27]. Park J, Bauer S, Mark K V D and Schmuki P 2007 *Nano Lett.* **7**, 1686.
- [28]. Prida V M, Manova E, Hernandex-Velez M, Aranda P, Pirota K R, Vazquez M, Ruiz-Hitzky E 2007, *J. Magn. Magn. Mater.* **316**, 110.
- [29]. Paulose M, Prakasam H E, Varghese O K, Peng L, Popat K C, Mor G K, Desai T A and Grimes C A 2007 *J. Phys. Chem. C* **111**, 14992.

- [30]. Park J, Kim S, and Bard A J 2006 *Nano Lett.* **6**, 24.
- [31]. Zhu K, Neale N R, Miedaner A and Frank A J 2007 *Nano Lett.* **7**, 69.
- [32]. Varghese O K, Gong D, Paulose M, Ong K G and Grimes C A 2003 *Sens. Actuators B* **93**, 338.
- [33]. Xiao P, Liu D, Garcia B B, Sepehri S, Zhang Y and Cao G 2008 *Sens. Actuators B* **134**, 367.
- [34]. Toledo-Antonio J A, Capula S, Corts-Jcome M A, Angeles-Chvez C, Lpez-Salinas E, Ferrat G, Navarrete J and Escobar J 2007 *J. Phys. Chem. C* **111**, 10799.
- [35]. Mor G K, Shankar K, Paulose M, Varghese O K and Grimes C A 2006 *Nano Lett.* **6**, 215.
- [36]. Funk S, Hokkanen B, Burghaus U, Ghicov A and Schmuki P 2007 *Nano Lett.* **7**, 1091.
- [37]. Oh S, Daraio C, Chen L, Pisanic T R and Fiñones R R, Jin S 2006 *J. Biomed. Mater Res. A* **78**, 97.
- [38]. S. P. Albu, A. Ghicov, J. M. Macak, R. Hahn and P. Schmuki, *Nano Lett.* **7**, 1286 (2007).
- [39]. Cahill D G and Allen T H 1994 *Appl. Phys. Lett.* **65**, 309.
- [40]. Guo J, Wang X and Wang T 2007 *J. Appl. Phys.* **101**, 063537.
- [41]. Wang T, Wang X, Zhang Y, Liu L, Xu L, Liu Y, Zhang L, Luo Z and Cen K 2008 *J. Appl. Phys.* **104**, 013528.
- [42]. Allen M P and Tildesley D J 1987 *Computer Simulation of Liquids* (Clarendon,

Oxford).

- [43]. Feng X and Wang X 2008 *Appl. Surface Sci.* **254** 4201-4210.
- [44]. Edens A D, Ditmire T, Hansen J F, Edwards J F, Adams R G, Rambo P, Ruggles L, Smith I C and Porter J L 2004 *Phys. Plasmas.* **11** 4968-72.
- [45]. Mendes M and Vilar R 2003 *Appl. Surface Sci.* **206** 196-208.
- [46]. Wang J and Lin Z 2009 *J. Phys. Chem. C*, **113**, 4026.
- [47]. Paulose M, Shankar K, Yoriya S, Prakasam H E, Varghese O K, Mor G K, Latempa T A, Fitzgerald A and Grimes C A 2006 *J. Phys. Chem. B* **110**, 16179.
- [48]. Dames C, Poudel B, Wang W Z, Huang J Y, Ren Z F, Sun Y, Oh J I, Opeil C, Naughton M J and Chen G 2005 *Appl. Phys. Lett.* **87**, 031901.
- [49]. Martan J, Herve O and Lang V 2007 *Journal of Applied Physics* **102** (6), 064903.
- [50]. Lee S M and Cahill D G 1995 *Phys. Rev. B* **52**, 253.
- [51]. Hou J, Wang X and Guo J 2006 *J. Phys. D: Appl. Phys.* **39**, 3362

RELATED PUBLICATIONS

1. L. Guo and X. Wang, 2008, "Effect of the Molecular Weight and Density of Ambient Gas on Shock Wave in Laser-assisted Nanostructuring," Proceedings of MicroNano08, MicroNano2008, June 3-5, 2008, Clear Water Bay, Kowloon, Hong Kong. Paper # 70178.
2. L. Guo and X. Wang, 2008, "Effect of Molecular Weight and Density of Ambient Gas on Shock Wave in Laser-induced Surface Nanostructuring," Journal of Physics D: Applied Physics, Vol. 42, 015307.
3. L. Guo, J. Wang, Z.Q. Lin, S. Gacek, and X. Wang, 2009, "Anisotropic Thermal Transport in Highly Ordered Amorphous TiO₂ Nanotube Arrays," (in review).